



PORPHYRY VECTORING TECHNIQUES IN ADVANCED ARGILLIC ALTERED ROCKS OF BRITISH COLUMBIA

Bouzari, F., Lee, R.G., Hart, C.J.R., and van Straaten, B.I.

Geoscience BC Report 2022-03

MDRU Publication 456

PORPHYRY VECTORING TECHNIQUES IN ADVANCED ARGILLIC ALTERED ROCKS OF BRITISH COLUMBIA

Farhad Bouzari¹, Robert G. Lee¹, Craig J.R. Hart¹, and Bram I. van Straaten²

Geoscience BC* Report 2022-03

MDRU Publication 456

¹ MDRU – Mineral Deposit Research Unit, The University of British Columbia, Canada

² British Columbia Geological Survey, British Columbia Ministry of Energy, Mines and Low Carbon Innovation, Victoria, British Columbia, Canada

Keywords: Porphyry Deposits Exploration, Advanced Argillic Alteration, Vectors, British Columbia

Suggested Citation:

Bouzari, F., Lee, R.G., Hart, C.J.R., and van Straaten, B.I. (2022): Porphyry Vectoring Techniques in Advanced Argillic Altered Rocks of British Columbia: Geoscience BC Report 2022-03, MDRU Publication 456, 38 p.

Report prepared by MDRU[†]

©2022 MDRU—Mineral Deposit Research Unit

Dept. Earth, Ocean and Atmospheric Sciences, The University of British Columbia

Vancouver, BC V6T 1Z4, Canada

Tel: +1-604-822-6136

Email: mdru@eoas.ubc.ca

Includes bibliographic references.

Electronic monograph issued in PDF format.

ISBN 978-0-88865-478-6

*Geoscience BC is an independent, non-profit organization that generates earth science in collaboration with First Nations, local communities, government, academia and the resource sector. Our independent earth science enables informed resource management decisions and attracts investment and jobs. Geoscience BC gratefully acknowledges the financial support of the Province of British Columbia.

[†]MDRU—Mineral Deposit Research Unit is an internationally-recognized collaborative venture between the mining industry and Earth, Ocean and Atmospheric Sciences Department at The University of British Columbia (UBC), established with assistance from the Natural Sciences and Engineering Research Council of Canada (NSERC), and devoted to solving mineral exploration-related problems.

Cover image: *Tanzilla lithocap, near Dease Lake, northern British Columbia, looking northeast to the north ridge from the Main zone hill characterized by silicified rock with intense topaz-pyrophyllite-muscovite alteration, limonite stained volcanic rock outcrops with muscovite alteration which transitions to muscovite-chlorite alteration distally.*

CONTENTS

ABSTRACT	1
INTRODUCTION	2
MINERALOGY AND ZONING OF ADVANCED ARGILLIC ALTERATION	2
GEOLOGICAL SETTING: ADVANCED ARGILLIC ALTERATION IN BC	3
<i>Tanzilla</i>	3
<i>Alunite Ridge</i>	4
<i>Kemess North</i>	6
SAMPLING AND ANALYTICAL WORK	7
ALTERATION MINERALOGY	9
<i>Tanzilla</i>	9
<i>Alunite Ridge</i>	9
<i>Kemess North</i>	12
CATHODOLUMINESCENCE OF ADVANCED ARGILLIC ALTERATION MINERALS	13
HOST ROCK COMPOSITION AND EFFECT ON ALTERATION	16
ALTERATION COMPOSITIONAL VECTORS	16
<i>Alkali-Alumina Diagram</i>	19
<i>K-Mg-Alumina Diagram</i>	20
<i>Advanced Argillic Alteration by K/Rb-Alumina Diagram</i>	21
GEOCHEMICAL VECTORS	22
<i>MDRU Porphyry Index (MPIx)</i>	22
<i>MDRU Porphyry Index-Lateral (MPIx-Lateral)</i>	24
<i>Na-Ca Depletion Index</i>	24
ROCK PHYSICAL PROPERTY VECTORS	24
<i>Magnetic Susceptibility</i>	26
<i>Rock Density</i>	26
<i>Rock Porosity</i>	27
DISCUSSION: MAPPING ADVANCED ARGILLIC ALTERATION ZONING	29
<i>Nodular Pyrophyllite and Aluminum-rich Minerals at the Core/Roots of Advanced Argillic Alteration</i>	30
<i>Transition from Green to White Muscovite</i>	31
<i>K-Mg-Alumina and K/Rb-Alumina Diagrams to Map Alteration</i>	31
<i>Rock Physical Properties</i>	32
<i>Trace Element Vectors: MPIx and MPIx- Lateral</i>	32
<i>Red Luminescent Quartz</i>	32
CONCLUSIONS	33
ACKNOWLEDGMENTS	33
REFERENCES	34
LIST OF APPENDICES	38

ABSTRACT

Zones of advanced argillic-alteration occur in the upper parts of porphyry copper systems, with a blanket-like geometry that, if preserved may create the largest near-surface footprint of the hydrothermal systems. These zones may host high-sulphidation epithermal-type gold deposits and/or conceal porphyry copper mineralization at depth. Mineral exploration within advanced argillic zones is difficult because of the large size of the altered areas, the intense nature of the alteration, and the subtle mineralogical changes that can be challenging to identify.

In this study, alteration-mineral assemblages and compositions across zones of advanced argillic alteration in three British Columbia (BC) mineral properties are characterized: Tanzilla (near Dease Lake) and the Alunite Ridge and Kemess North mineral properties (both in the Toodoggone district). A total of 230 rock samples were collected that represent various alteration assemblages from the zone of advanced argillic alteration to 5–6 km outside the zone of intense alteration. These samples were characterized by field observations, hyperspectral shortwave infrared (SWIR), petrography, cathodoluminescence, scanning-electron microscope (SEM), physical rock properties (including magnetic susceptibility, density, and porosity) as well as whole-rock major and trace element compositions.

Aluminum-rich minerals such as andalusite, corundum, diaspore, and topaz occur within zones of intense alteration and silicification (residual and added quartz) with pyrophyllite and/or muscovite-clay assemblages. The muscovite colour changes laterally, with respect to the main up-flow zone, to pale-green and green, in conjunction with a change to more phengitic composition. A new K-Mg-Al molar diagram is introduced to map white muscovite-clay-(aluminum-rich minerals), pale-green muscovite, green muscovite-chlorite, and chlorite-dominated alteration assemblages. A K/Rb-Al molar diagram is introduced that distinguishes the aluminum-rich phases from those of the muscovite-clay assemblages to identify vectors within the zones of advanced argillic alteration. Cathodoluminescence study indicates that quartz within more central parts of advanced argillic alteration displays red luminescence and typically occurs with blue luminescent pyrophyllite and clays.

Two trace element indices (Mineral Deposit Research Unit – MDRU Porphyry Index (MPIx) and MPIx-Lateral) are used to map the mineralization footprints vertically and laterally. These indices provide tools to compare prospects in a district, identify size and level of exposure, and help target drilling. A Na-Ca depletion index helps map the intensity of muscovite and advanced argillic-alteration, adding tools for defining vectors for mineralization. Measured physical rock properties correlate with the type and intensity of alteration.

These observations provide a toolset that can aid rapid and cost-effective exploration vectoring for porphyry copper and related epithermal mineralization within and around advanced argillic altered rocks in British Columbia and elsewhere.

INTRODUCTION

Zones of advanced argillic alteration in the upper parts of porphyry copper systems, also known as ‘lithocaps’ (Sillitoe, 1995), can have a blanket-like geometry with areal extents of >10 km². They may be as thick as 1 km and, where preserved, form the largest near-surface footprints of porphyry copper systems (Sillitoe, 2010; Hedenquist and Taran, 2013; Cooke et al., 2017; Hedenquist and Arribas, 2021). Large, coalesced zones of advanced argillic may underline two or more porphyry copper deposits (Sillitoe, 1999; 2010). Lithocaps may themselves host high-sulphidation epithermal-type gold deposits if they are preserved from erosion (e.g., Yanacocha; Longo et al., 2010).

Mineral exploration within advanced argillic zones is traditionally difficult because of the large size of the altered areas, the intense nature of the alteration, and the subtle mineralogical changes that can be difficult to identify in the field or with tools such as a hand lens. More importantly, shallow parts of advanced argillic alteration, the quartz-alunite zone, for example, are commonly offset from their causative intrusions that typically host porphyry copper deposits, such as the Lepanto lithocap in the Philippines (Hedenquist et al., 1998). The offset is caused by cooling along shallow hydraulic gradients away from intrusive centres (Hedenquist and Taran, 2013). Therefore, characterizing the textural, mineralogical, and geochemical trends around and within these zones of advanced argillic alteration is essential for explorers to identify proximity indicators of potential high-sulphidation epithermal gold and underlying porphyry deposits.

Porphyry copper deposits comprise a large range of the metal tenor, including both grade and payable elements, and a corresponding diversity of parageneses and fabrics (e.g., Clark, 1993). They commonly have large alteration and geochemical footprints (e.g., Titley et al., 1986; Cunningham et al. 2004; Halley et al., 2015; Byrne et al., 2020). Advances in obtaining high-quality whole-rock geochemical data for exploration (e.g., Halley, 2020; Barker et al., 2021), as well as textural and mineral mapping by shortwave infrared techniques (SWIR: Lypaczewski et al., 2020; Byrne et al., 2020; Portela et al., 2021), provide an improved framework for vectoring within zones of advanced argillic alteration. In addition, traditional petrography (Watanabe and Hedenquist, 2001), backed by cathodoluminescence studies (e.g., Maydagán et al., 2015; Rusk et al., 2006; Bennett, 2014; Holley et al., 2017) provide an opportunity to further delineate complex alteration zones in advanced argillic rocks and improve techniques for decision making during exploration targeting.

In this study, alteration mineral assemblages and rock compositions across advanced argillic-alteration zones in three British Columbia (BC) mineral properties are characterized: the Tanzilla mineral property, near Dease Lake, and the Alunite

Ridge and Kemess North mineral properties, both in the Toodoggone district. Rocks were sampled within the zones of advanced argillic-altered rocks, and up to 5–6 km outside of the zone of intense advanced argillic alteration in the surrounding rocks that typically had muscovite and chlorite alteration. Alteration mineral assemblages were characterized by field observations, hyperspectral SWIR, petrography assisted by cathodoluminescence (CL), and scanning electron microscope (SEM) imaging. These data were supplemented by measurements of rock physical properties, including magnetic susceptibility, density, and porosity. Whole-rock major and trace element data were used to map trace element vectors and compare them with alteration mineralogy.

Results show alteration zoning of 16 mineral assemblages within and around zones of advanced argillic-altered rocks. A new K-Mg-Al diagram is introduced to map alteration assemblages in four groups based on whole-rock analyses. This is supplemented by a K/Rb-Al diagram, which distinguishes aluminous-rich and alunite-rich assemblages from muscovite-clay (kaolinite, dickite) altered zones. Additionally, trace element data are used to establish geochemical indices, which can provide both horizontal and vertical vectors in and around porphyry-related alteration. Cathodoluminescence imaging is used to characterize and distinguish various types of quartz occurring with the advanced argillic alteration. These findings are used to provide a toolset for rapid and cost-effective exploration vectoring for porphyry copper and related epithermal mineralization within and around zones of advanced argillic-altered rocks.

MINERALOGY AND ZONING OF ADVANCED ARGILLIC ALTERATION

Advanced argillic alteration occurs in shallow geological environments where sulfate-bearing and/or aluminosilicate minerals indicate formation by reactive fluids (Hedenquist and Arribas, 2021). The advanced argillic alteration was defined by Meyer and Hemley (1967) to refer to hydrothermal alteration that may include “dickite, kaolinite, pyrophyllite, usually with sericite, quartz, and frequently alunite, pyrite, tourmaline, topaz, zunyite, and amorphous clays”. Andalusite and corundum may also be included in this association (Hemley et al., 1980). Zones of advanced argillic alteration are typically characterized by quartz-alunite veins and residual quartz with halos of kaolinite±dickite and roots of pyrophyllite±diaspore (Figure 1, *after* Sillitoe, 2010). These are formed by an early stage of intense acid leaching of the wall rocks, which results from magmatic SO₂ and HCl vapours that condense into groundwater and cool below 300°C resulting in the dissociation of strong acids such as HCl or H₂SO₄ (Hedenquist and Taran, 2013; Hedenquist and Arribas, 2021). A second stage of post-vapour fluid deposits the bulk of the sulphide minerals and

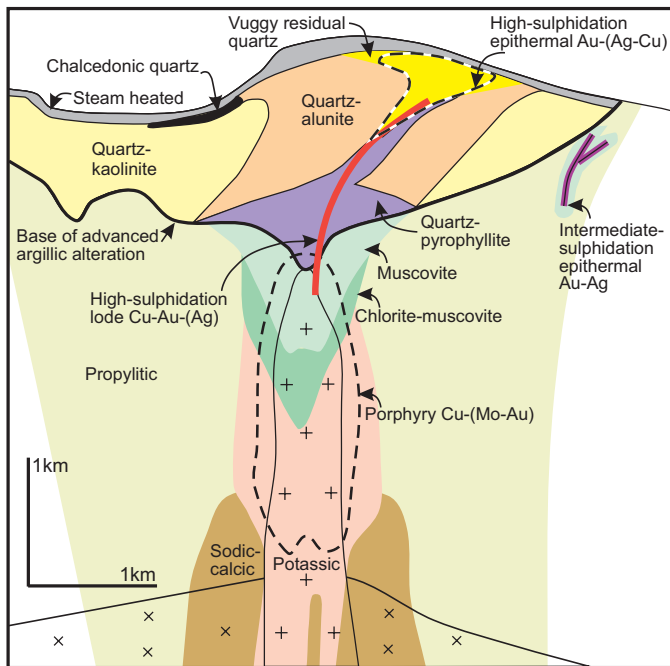


Figure 1: Schematic cross-section showing main components of advanced argillic alteration above porphyry mineralization (after Sillitoe, 2010).

precious metals with euhedral quartz precipitate (Stoffregen, 1987; Heinrich et al., 2004; Heinrich, 2007; Holley et al., 2017). Additionally, boiling of a hydrothermal liquid generates vapor with CO_2 and H_2S rich vapor, which condenses into groundwater and forms sulfuric acid and steam-heated acid-sulfate alteration (Hedenquist and Arribas, 2021). Zones of advanced argillic alteration characteristically flare upward along feeder structures and form a sub-horizontal blanket if a permeable lithologic unit is intersected (Steven and Ratté, 1960; Hedenquist and Taran, 2013).

Similar to the deeper alteration in porphyry deposits, the advanced argillic assemblages are typically zoned from quartz-pyrophyllite at depth to quartz-alunite and residual quartz with a vuggy appearance at a shallower level (Sillitoe, 1995, 2010; Hedenquist et al., 1998). Minerals such as diaspore and andalusite with pyrophyllite and/or muscovite occur in the upper portions of the porphyry deposit (Sillitoe, 1995, 2010; Hedenquist et al., 1998; Watanabe and Hedenquist, 2001; Chang et al., 2011; Cooke et al., 2017; Hedenquist and Arribas, 2021). These minerals form from the cooling of high-temperature, initially muscovite-stable fluids ($\approx 370^\circ\text{C}$; Hemley et al., 1980; Hedenquist and Taran, 2013), as observed at El Salvador and Cerro Colorado, Chile (Watanabe and Hedenquist, 2001; Bouzari and Clark, 2006). Fluorine-rich fluids produce topaz, zunyite, and fluorite (e.g., Hugo Dummett deposit, Oyu Tolgoi mineral district, Mongolia; Khashgerel et al., 2008); the former two minerals are included in the advance argillic definition (Meyer and Hemley, 1967).

Advanced argillic alteration in some porphyry deposits overprints earlier and deeper porphyry alteration. This may be due to “telescoping” (Sillitoe, 2010) caused by rapid uplift and erosion of the volcanic edifice, or by overprinting of an older, eroded system by a younger system (e.g., Escondida deposit, Chile, overprinted by quartz-alunite related to the younger intrusion of the deeper Escondida Este: Hervé et al., 2012). Therefore, identification and characterization of advanced argillic alteration and distinction from pre-existing higher temperature alteration or adjacent propylitic assemblage are critical to establish the vertical profile of the system and the potential for hypogene mineralization at depth.

GEOLOGICAL SETTING: ADVANCED ARGILLIC ALTERATION IN BC

Advanced argillic alteration is a relatively uncommon feature in many known porphyry deposits in British Columbia; this is widely attributed to the level of erosion of these older deposits that has removed the shallow parts of porphyry systems in many districts. However, advanced argillic alteration is preserved in some locations in BC, particularly within districts that are prospective to host porphyry-type copper deposits. Zones of advanced argillic alteration areas are present in northern BC and northern Vancouver Island. Studies in the Toodoggone district (Bouzari et al., 2020), the Bonanza volcanic field in northern Vancouver Island (Panteleyev and Koyanagi, 1994), Limonite Creek in central BC (Deyell et al., 2000), and several other locations in BC have recognized linkages between advanced argillic alteration and porphyry-type mineralization at depth.

Tanzilla, Alunite Ridge, and Kemess North are located in the Stikine terrane of northern BC (Figure 2). The geological setting and mineral occurrences of these mineral properties have been described in several previous studies (e.g., Diakow et al., 1991, 1993, 2006; van Straaten and Gibson 2017; Bouzari et al., 2020), and brief summaries are provided here.

Tanzilla

The Tanzilla property is within the Intermontane belt, near the northeastern margin of the Stikine terrane (Figure 2), a Late Triassic–Early Jurassic volcanic island-arc complex accreted to ancestral North America during the Middle Jurassic (Nelson and Mihalynuk, 1993). The Tanzilla property is underlain by a volcanic succession assigned to the Horn Mountain Formation (late Early to Middle Jurassic; van Straaten and Nelson, 2016) in the upper part of the Hazelton Group (Figure 3). The lower part of the Horn Mountain Formation includes massive green augite-plagioclase-phyric volcanic breccia (not exposed in the study area), whereas the middle part is mainly maroon coloured volcanic breccias, autobreccias, and flows, and includes minor

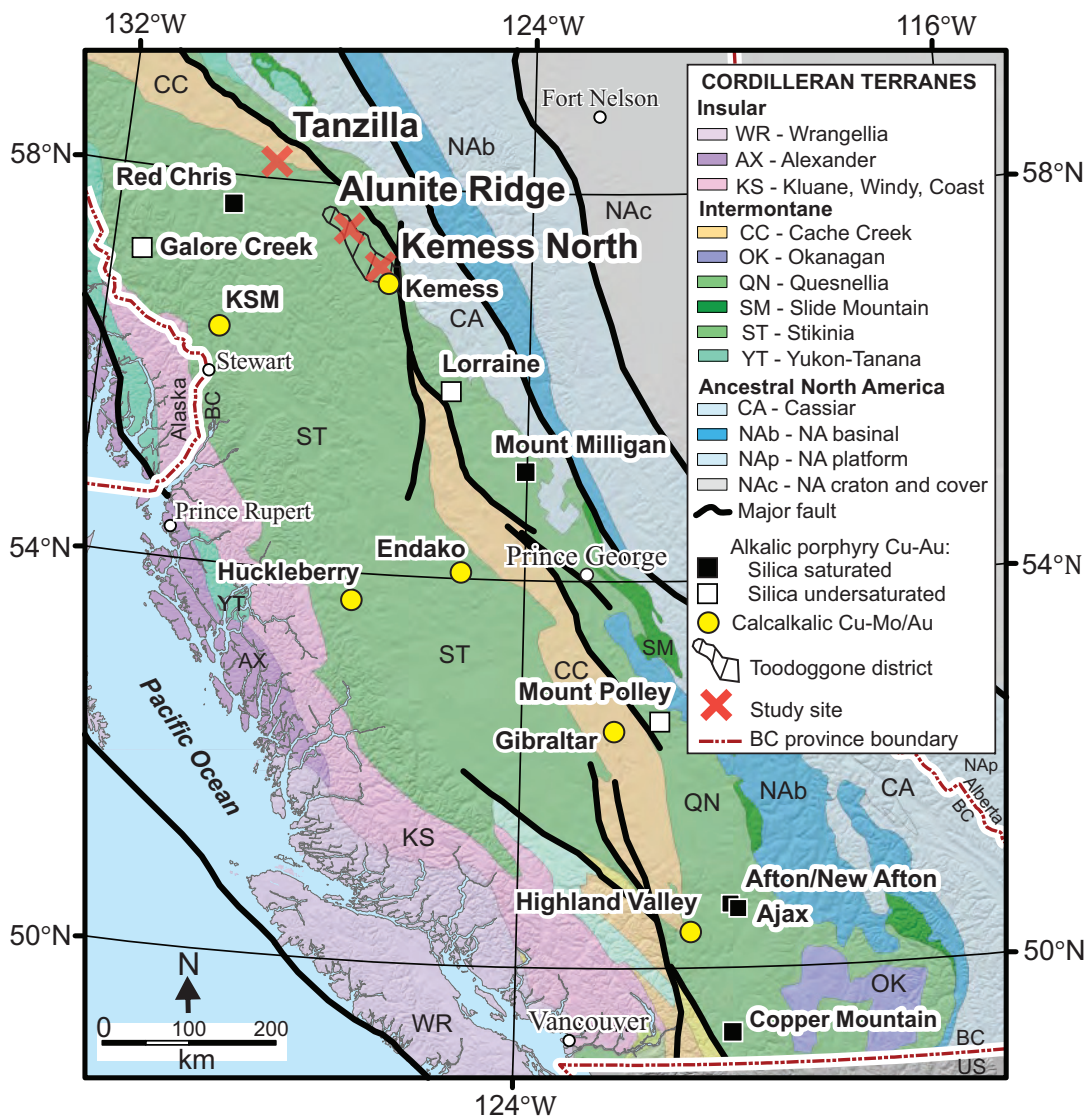


Figure 2: Cordilleran terranes of British Columbia with the location of the study areas (after Bissig and Cooke, 2014).

laminated felsic tuffs to bedded lapillistone. The upper parts of the Horn Mountain Formation consist of a felsic volcanic unit of mainly aphanitic and plagioclase-phyric clasts capped by a mafic volcanic unit of augite-plagioclase-phyric volcanic breccia and flows (van Straaten and Gibson, 2017). These units are unconformably overlain by sedimentary rocks of the Bowser Lake Group. The Late Jurassic Snowdrift Creek pluton cuts the Horn Mountain strata and the Kehlechoa thrust fault.

The Horn Mountain Formation hosts areally extensive advanced argillic-alteration at the Tanzilla-McBride property for at least 17 km along strike (van Straaten and Gibson, 2017; van Straaten and Bouzari, 2018). At Tanzilla, the zone of advanced argillic alteration is at least 5 x 2 km in size at the surface (Figure 3) and overlies porphyry-style alteration at depth, which is characterized by quartz-sericite-pyrite to K-silicate alteration (K-feldspar) with anomalous copper and molybdenum, hosted

by a plagioclase porphyry intrusion dated at 173 Ma (van Straaten and Nelson, 2016; van Straaten and Gibson, 2017).

Alunite Ridge

Alunite Ridge is located within the Toodoggone district of northeastern BC (Figure 2). The district hosts several Early Jurassic epithermal-type deposits with associated advanced argillic alteration (Diakow et al., 1993; Duuring et al., 2009; Bouzari et al., 2020). These deposits are hosted by a thick (>2 km) succession of Early Jurassic subaerial andesitic and dacitic volcanic rocks of the Toodoggone Formation (lower part of the Hazelton Group; Diakow et al., 1993). These and older strata were probably covered by thick successions (>4 km) of Jurassic and Cretaceous Bowser and Sustut basin clastic strata that helped to preserve the epithermal deposits during subsequent, post-Late Cretaceous uplift (Bouzari et al., 2020).

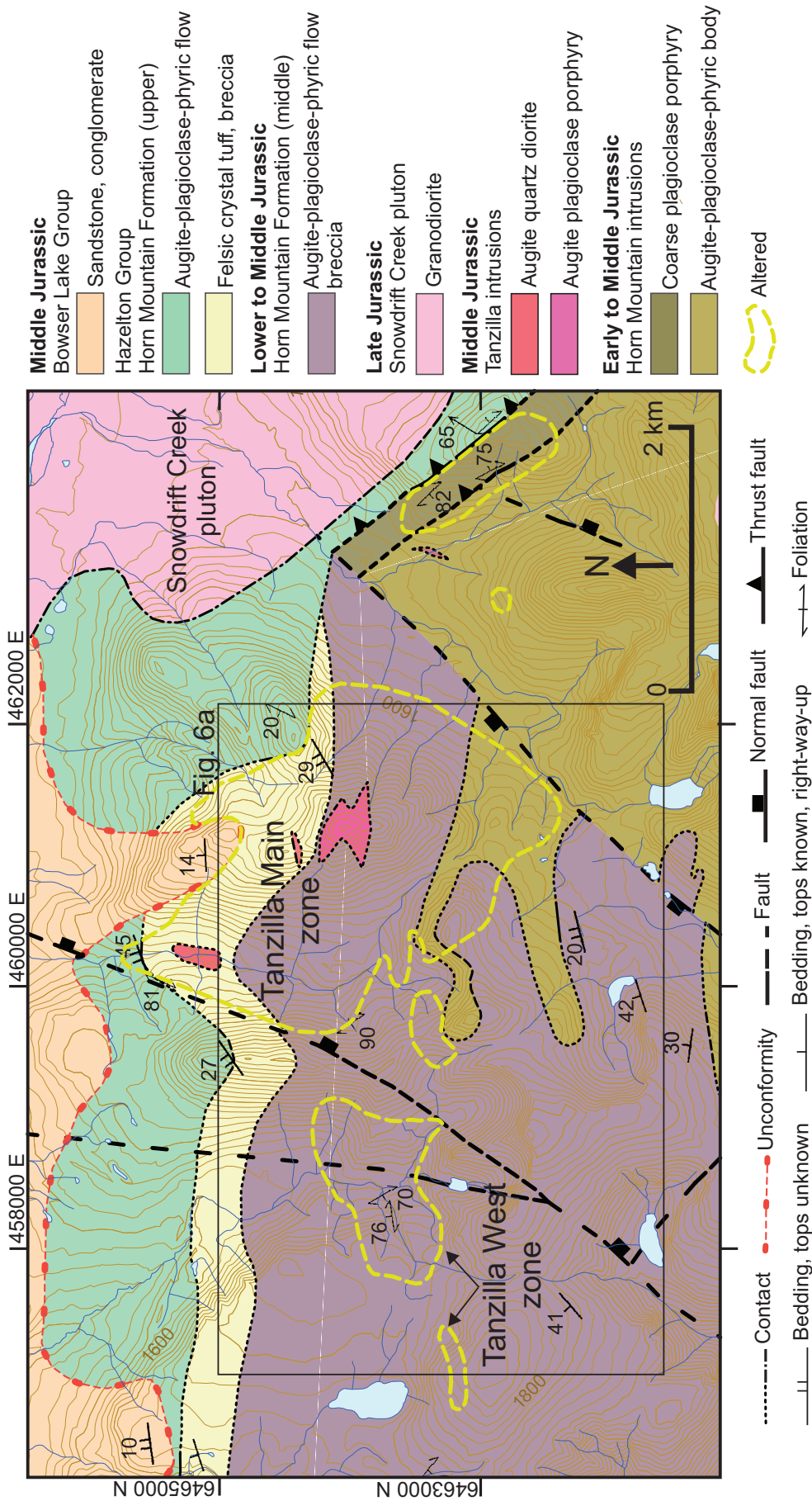


Figure 3: Geology of the Tanzilla study area (after van Straaten et al., 2017).

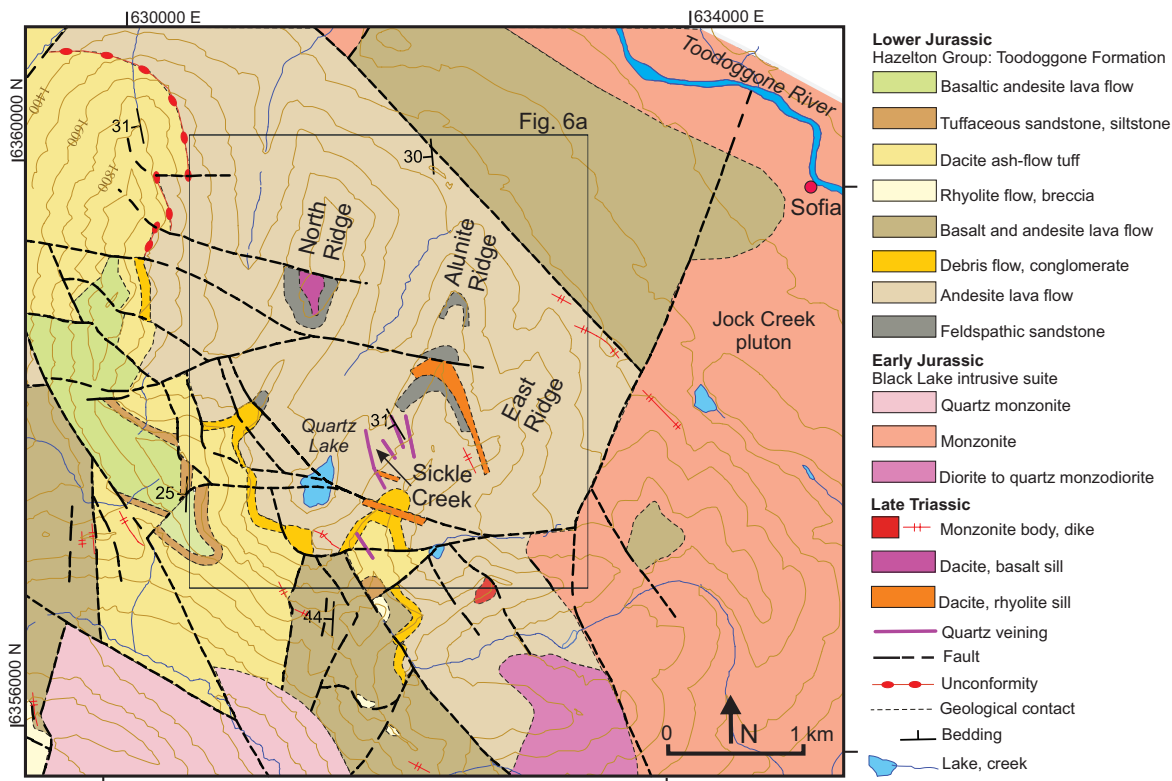


Figure 4: Geology of the Alunite Ridge study area (after Diakow et al., 2006).

The Alunite Ridge area near Quartz Lake hosts several mineral occurrences, including Quartz Lake, Alunite Ridge, North Ridge, and Sickle Creek (Figure 4). The bedrock geology consists of the Lower Toodoggone Formation (Early Jurassic), which is coeval with the Telkwa Formation of the Hazelton Group (Diakow et al., 1993), and consists of andesitic lava flows, tuff, breccia, and epiclastic rocks that are intruded by small dikes and stocks of monzonite (Figure 4). The Early Jurassic Jock Creek monzonitic pluton forms a large body to the south and east. Zones of intense alteration are northwest-trending and about 200 m wide. Gold mineralization occurs in a 10–15 m wide zone of silicified rock with quartz-alunite alteration (Duuring et al., 2009), locally with vuggy residual textures and zones of buff-grey intense diaspore alteration (Bouzari et al., 2020). Banded quartz veins with calcite and K-feldspar host low-to-intermediate sulphidation-type epithermal chalcopyrite-sphalerite-galena-pyrite mineralization and occur 200–300 m south of the advanced argillic-altered zone at Alunite Ridge and at the base of the valley near Quartz Lake.

Post-mineralization monzonite dikes cut the alteration. A small granodiorite body at the Sofia prospect in the Toodoggone River valley is about 3 km northeast of Alunite Ridge (Figure 4), at an elevation of 1050 m asl (i.e., 700 m lower than Alunite Ridge). The granodiorite at Sofia hosts quartz-magnetite veins with K-feldspar alteration with chalcopyrite, typical of deeper level porphyry mineralization (Bouzari et al., 2020).

Kemess North

The Kemess North porphyry is located about 6.5 km north of the main Kemess deposit (Kemess South) in the southern part of the Toodoggone district (Figure 2). Host rocks at Kemess North include Upper Triassic Takla Group andesite/basaltic volcanic rocks, locally overlain by Lower Jurassic Toodoggone Formation dacitic fragmental volcanic rocks (Figure 5). Toodoggone Formation volcanoclastic rocks crop out as prominent north-trending ridges or as isolated, fault-bounded blocks within Takla Group basalt. Several Early Jurassic stocks or dikes of quartz monzonite to quartz rhyolite composition of the Early Jurassic Black Lake intrusive suite have intruded the volcanic succession. The area is dominated by horst-and-graben-style normal faulting, south-dipping thrust faults, and southwest-dipping dip-slip faults (SRK Consulting Inc., 2016).

Porphyry-type veins and sulphide mineralization (Re-Os molybdenite age of 201.8 ± 1.2 Ma; McKinley, 2006) are centred around a quartz diorite body (ca. 202 Ma). The east-trending, south-dipping mineralization appears to have formed along faults. The present near-surface alteration, characterized by fine-grained quartz muscovite-chlorite-pyrite with zones of andalusite-corundum-pyrophyllite, grades with increasing depth to K-silicate alteration characterized by quartz-magnetite stringers with a decrease in the pyrite to chalcopyrite ratio.

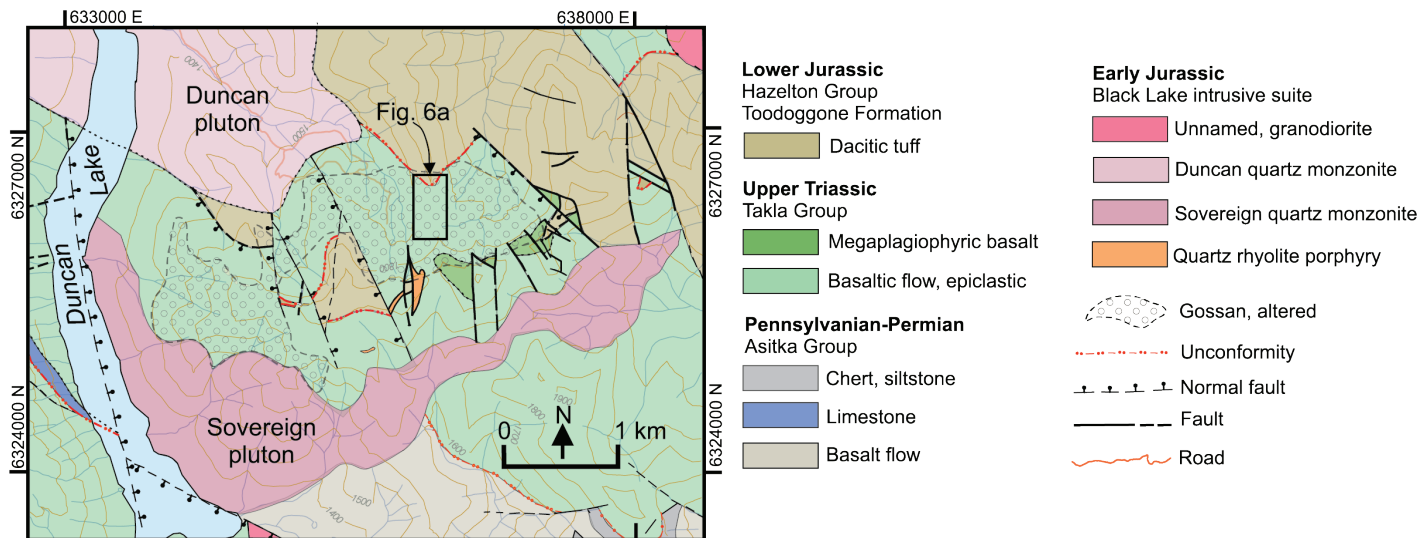


Figure 5: Geology of the Kemess North study area (after Diakow, 2001).

SAMPLING AND ANALYTICAL WORK

At Tanzilla, the advanced argillic alteration was mapped and sampled across a 3.5 km north-south profile and a 4 km east-west profile. A total of 54 samples were collected from surface outcrops. Drillhole TZ15-01 (Barresi and Luckman, 2016), which tested mineralization below the Main zone hill to the length of 840 m (-60°), was examined, and 20 core samples were collected to characterize alteration and mineralization at depth. At Alunite Ridge, the footprint of alteration was mapped and sampled along three northeast-trending profiles with a total length of approximately 5 km in an area of 2 x 2 km. In total, 63 samples from surface outcrops, ranging in elevation from 1908 to 1560 m asl and 10 samples from drill hole SG-04-18 (Kuran and Barrios, 2005) to a depth of 227 m below surface (1642 m asl) were collected. At Kemess North, the advanced argillic alteration was mapped and sampled along a north-south profile of approximately 0.5 km. In total, 18 samples were collected from surface outcrops. Drill holes KN-01-12 and KN-02-09 (SRK Consulting Inc., 2016), which tested mineralization below the advanced argillic alteration to a depth of ~500 m below surface, were examined, and 44 core samples were collected to characterize alteration and mineralization at depth. Surface sample locations are shown in Figure 6a, and a list of all samples with their coordinate locations and field descriptions is provided in Appendix 1.

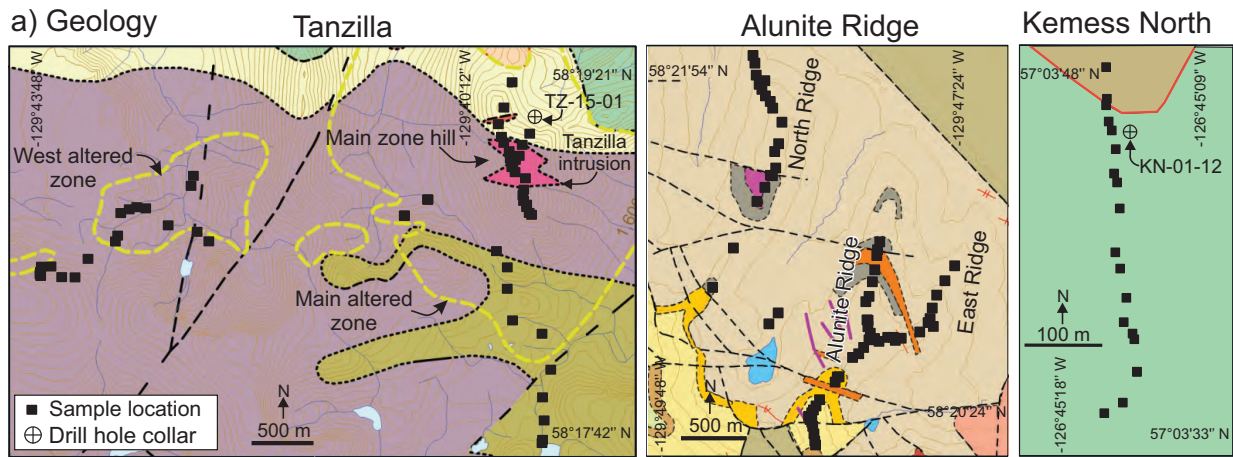
All rock samples were described in the field and again after being cut into slabs. To characterize alteration assemblages on the hand sample scale, all cut samples and half drill core samples were analyzed by shortwave infrared (SWIR) hyperspectral imagery, in the 1000 to 2500 nm range, using a Specim SisuROCK hyperspectral scanner (a line-scan imager) at the University of Alberta, Edmonton. The hyperspectral instrument contains a 256 spectral by 320 spatial pixels mercury-cadmium-telluride

(MCT) detector array that acquires data with a 6.3 nm sampling interval and a 10 nm spectral bandwidth. The instrument was equipped with an OLES56 lens, which yielded a spatial resolution of 0.2–0.5 mm/pixel.

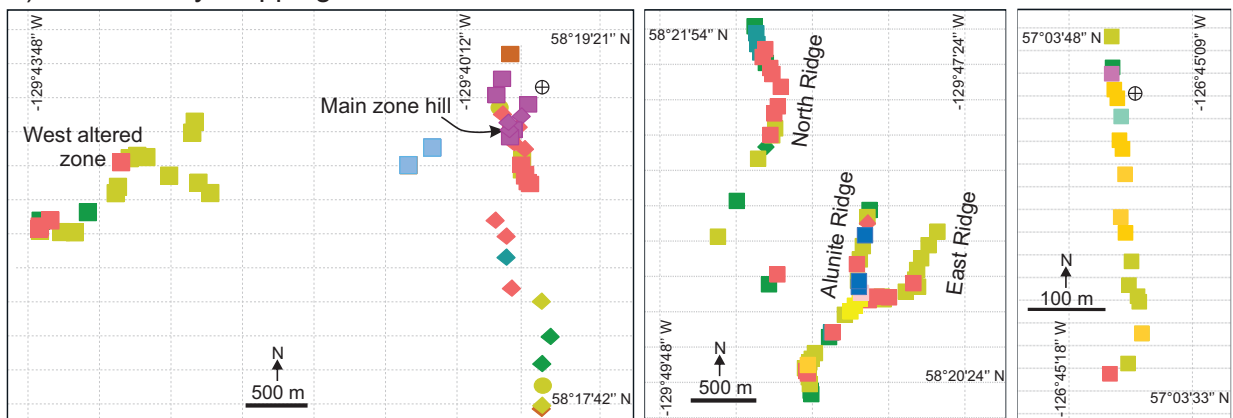
Details of hyperspectral data acquisition and interpretation are summarized in Lypaczewski et al. (2020). Hyperspectral data are shown in Appendix 2, and results of identified minerals from hyperspectral data with their relative abundance are shown on maps in Appendix 3.

Petrographic thin sections of 56 selected rock samples were examined to supplement the alteration study. Additionally, all polished thin sections were studied with a Cambridge Image Technology Ltd MK 4A model cold cathodoluminescence (CL) stage mounted on a petrographic microscope to further characterize alteration minerals. The samples were irradiated in a vacuum chamber with an electron beam of approximately 18 kV and the current set at 350–500 μ A. Selected samples were analyzed by SEM to confirm the mineralogy and composition.

A total of 223 whole-rock samples were analyzed for major- and trace- elements at Bureau Veritas Minerals (Vancouver, BC). Samples were crushed to 70% (-2 mm) and then riffle split and pulverized to 85% (75 μ m) using a ceramic bowl with silica wash between samples. Samples were analyzed by X-ray fluorescence (XF700 method) for SiO_2 , Al_2O_3 , Fe_2O_3 , CaO , MgO , Na_2O , K_2O , MnO , TiO_2 , P_2O_5 , Cr_2O_3 , SO_3 , and Sr; inductively coupled plasma (ICP)-mass spectrometry using lithium borate fusion (LF100) for Ba, Be, Co, Cs, Ga, Hf, Nb, Rb, Sn, Sr, Ta, Th, U, V, W, Zr, Y, La, Ce, Pr, Nd, Sm, Eu, Gd, Tb, Dy, Ho, Er, Tm, Yb, and Lu; multi-acid digestion followed by ICP-emission spectrometry and ICP-mass spectrometry (MA200) for Mo, Cu, Pb, Zn, Ag, Ni, As, Cd,

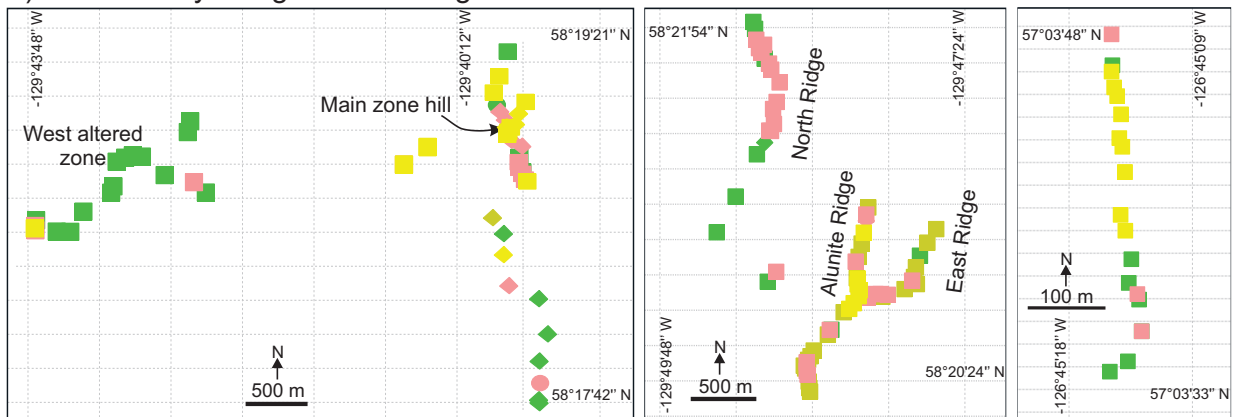


b) Alteration by mapping and SWIR



- biotite-chlorite ● chlorite ● chlorite-epidote-(muscovite) ● muscovite-chlorite ● muscovite-chlorite-kaolinite/dickite
- muscovite ● muscovite-kaolinite/dickite ● kaolinite/dickite ● kaolinite-dickite-diaspore ● topaz-pyrophyllite-muscovite
- topaz-kaolinite-muscovite ● alunite-topaz ● alunite ● andalusite-corundum-pyrophyllite-muscovite
- andalusite-corundum-muscovite-kaolinite/dickite ● volcanic ● intrusive, porphyry ● intrusive, equigranular

c) Alteration by K-Mg-Alumina diagram



- Group A (chlorite) ■ Group B (muscovite-chlorite) ■ Group C (muscovite) ■ Group D (clay, aluminum-rich minerals)

Figure 6: Location of samples from the Tanzilla, Alunite Ridge, and Kemess North study areas: a) distribution relative to the regional geology (see Figures 3, 4, and 5 for the legend of geological units); b) distribution of alteration-mineral assemblages identified by hand-lens, thin-section petrography, and shortwave-infrared analyses; and c) alteration assemblages characterized by K-Mg-Alumina diagram using whole-rock geochemical data.

Sb, Bi, Sc, Se and Tl; and Au by fire assay/atomic absorption spectroscopy. The portion of dried sample was roasted at 1000°C to determine the loss on ignition (LOI). All geochemical data are available in Appendix 4.

The magnetic susceptibility of all collected rocks was measured with a KT-10 magnetic susceptibility meter manufactured by Terraplus Inc. For each sample, five measurements were collected, and an average was used for interpretations. Rock density and porosity of all collected rocks were measured using saturation and buoyancy techniques (Ulusay and Hudson, 2007) at MDRU. All rock physical property data are available in Appendix 5. Table 1 shows analytical data for a representative set of samples.

ALTERATION MINERALOGY

Alteration mineral assemblages were mapped across the studied sites using the collected sample suites. Mineral phases identified by SWIR hyperspectral analyses and their relative abundance are displayed on maps in Appendix 2. The percentage of minerals shown on these maps is the relative abundance of mineral phase calculated on the basis of pixel count of a single mineral, i.e., pixels with the current mineral divided into the total rock pixels. The SWIR data of minerals with abundance greater than 5%, backed by field and petrography mineralogical data, were used to characterize and categorize alteration mineral assemblages in each sample, and these are shown in Figure 6b. Andalusite and corundum were specifically identified by petrography. Distribution and mineralogical trends are discussed below for each of the studied sites.

As described by Lypaczewski et al. (2020), certain alteration minerals such as muscovite, illite, and montmorillonite occur as intimate mixtures (on micro-scale) and therefore cause spectral mixing. In this study, the Al-rich phase identified as muscovite locally shows variably developed 1467 nm and 1900 nm absorption, which may indicate coexisting montmorillonite and/or illite. Therefore, the term 'white mica' is more appropriate to use a group name, which includes illite and muscovite; illite is deficient in K and Al but has more Si than muscovite (Al:Si 1:1). Alternatively, the name sericite has been widely used as a field term to designate fine-grained white mica (Meyer and Hemley, 1967). In this study, we used muscovite rather than white mica because we noted that muscovite (locally variably mixed with illite) displays different colours such as green, pale green, or white. This simplification helps to avoid mixing the colour of the phase (e.g., white or green) with the name of the group (white mica).

Tanzilla

At Tanzilla, advanced argillic-alteration covers a surface area of 5 × 2 km on the western margin of the Snowdrift Creek pluton

(Figure 3, van Straaten and Nelson, 2016). The main Tanzilla hill alteration occurs in an area of 2 × 2 km (Figures 3, 6a, 7a), referred to here as the Main zone. Similar types of alteration zones occur 2–3 km to the west, referred to here as the West zone. Field and SWIR data show that alteration at Tanzilla is characterized by a green muscovite-chlorite assemblage (Figure 7f) that grades, toward the zones of advanced argillic alteration at the hill in the Tanzilla Main zone, to a muscovite-dominated phase with pale green to white colour typically with the greater silicification (Figures 6b, 7e). In more central locations and commonly at higher elevations, the alteration is characterized by highly silicified rock with remnant muscovite, pyrite (jarosite), and abundant pyrophyllite and topaz (Figure 7a) locally with andalusite and minor corundum, the latter two minerals were identified in thin section (Figure 7b). Alunite occurs with topaz in zones at lower elevation in a valley west of the Main hill (Figures 6b and 7d). Alteration outside of the green muscovite-chlorite assemblage zone is dominantly darker green chlorite-muscovite (Figure 7g); in more distal locations, patchy chlorite-epidote alteration occurs within the volcanic rocks (Figure 6b). The chlorite alteration is pervasive and locally alters an earlier phase of biotite alteration with remnants of biotite altered to chlorite and fine-grained rutile based on thin-section petrography.

SWIR data shows that both paragonitic muscovite and muscovite are common at Tanzilla, whereas phengitic muscovite is rare (Figure 8a). The muscovite crystallinity index, calculated from the ratio of 2200 nm and 1900 nm wavelength depths of SWIR data, indicates that muscovite in the Tanzilla Main zone is highly crystalline (>2.0), whereas further south and at the West zone, samples are less crystalline (<1.5; Figure 8b).

Alunite Ridge

Advanced argillic alteration in the Alunite Ridge area occurs for over 2 km along a north-northeast-trending ridge (Alunite Ridge) and extends further to the north along North Ridge and the east along the East Ridge (Figures 4, 6b, 9a). Field observations, backed by petrography and SWIR data, indicate that the central parts of the Alunite Ridge property are characterized by an alteration zone of strong silicification with alunite, kaolinite, dickite, and locally diaspore (Figures 6b, 9b and 9c). This zone is surrounded by an alteration zone of silicification with white muscovite (Figure 9d), which gradually transitions to the north and east to alteration of green muscovite with remnants of chlorite (Figure 9e), and more distal to the central parts of Alunite Ridge, chlorite (Figure 7g), locally with epidote (Figure 9f). K-rich muscovite is common, and both paragonitic and phengitic compositions locally occur (Figure 8a). Muscovite crystallinity is typically low at Alunite Ridge (<1), especially in distal locations based on SWIR (Figure 8b).

Table 1, continued: Representative whole-rock, physical property and hyperspectral analyses data

Sample#	Unit	Method	Alunite Ridge										Kemess North					Tanzilia		
			19FB-101	19FB-087	19FB-115	19FB-098	19FB-073	19FB-080	19FB-124	19FB-127	19FB-132	19FB-131	19FB-040	19FB-027	19FB-016	1Z-15-01-164	19FB-053B			
Gd	ppm	LF100	4.73	1.94	3.81	0.77	1.21	0.8	1.96	1.88	1.79	0.76	4.13	4.56	0.71	1.01	4.04			
Tb	ppm	LF100	0.69	0.3	0.57	0.16	0.1	0.11	0.28	0.33	0.27	0.1	0.61	0.69	0.11	0.15	0.6			
Dy	ppm	LF100	3.93	1.77	3.38	1.11	0.44	0.67	1.6	2.05	1.74	0.62	3.36	4.07	0.8	0.84	3.56			
Ho	ppm	LF100	0.85	0.4	0.71	0.29	0.11	0.15	0.36	0.49	0.37	0.12	0.7	0.82	0.17	0.15	0.82			
Er	ppm	LF100	2.37	1.29	2.21	1.04	0.47	0.61	1.09	1.54	1.18	0.39	1.94	2.54	0.57	0.47	2.59			
Tm	ppm	LF100	0.33	0.2	0.3	0.17	0.09	0.1	0.15	0.24	0.17	0.07	0.29	0.36	0.08	0.06	0.43			
Yb	ppm	LF100	2.27	1.52	2.11	1.27	0.85	0.77	1.07	1.59	1.21	0.71	1.74	2.42	0.53	0.52	2.94			
Lu	ppm	MA200	0.37	0.27	0.35	0.22	0.15	0.15	0.17	0.27	0.19	0.13	0.26	0.39	0.07	0.09	0.48			
Mo	ppm	MA200	<DL	<DL	1.3	4	3.7	7.6	2.5	7.1	1	2.5	2.4	1	1.8	32.5	5.6			
Cu	ppm	MA200	3.7	2.4	12.8	4.8	2.2	8.7	21.6	21.6	14	20	109.6	14.7	20.6	19.1	39.8			
Pb	ppm	MA200	3.5	6.1	11.9	7.9	148.5	303.9	23.4	19.5	20.1	18.3	6.6	29.8	8.8	14.9	22.5			
Zn	ppm	MA200	114	85	856	3	<DL	16	162	11	10	11	42	175	5	2	1			
Ag	ppm	MA200	<DL	<DL	<DL	<DL	0.3	1.8	0.7	0.5	0.1	0.2	<DL	0.2	0.3	<DL	<DL			
Ni	ppm	MA200	8.7	0.9	2.8	0.1	<DL	0.1	22.5	4.6	<DL	6.6	6.2	0.3	0.3	2	2.1			
As	ppm	MA200	1	1	3	6	<DL	216	2	<DL	2	1	9	5	6	3	14			
Cd	ppm	MA200	0.2	<DL	5.4	<DL	0.2	0.7	<DL	<DL	<DL									
Sb	ppm	MA200	0.3	1	0.5	3.9	2.6	92.7	0.3	0.3	1.7	0.9	1.7	0.8	1.5	0.8	3.5			
Bi	ppm	MA200	<DL	<DL	<DL	0.9	0.4	14.7	0.4	0.8	0.3	0.6	0.1	<DL	0.2	0.8	1.1			
Sc	ppm	MA200	23	4	12	4	8	8	16	17	3	6	22	7	<DL	2	10			
Se	ppm	MA200	<DL	<DL	<DL	1	<DL	1	1.9	9	2	11	1	3	<DL	3	9			
Ti	ppm	MA200	<DL	<DL	1	<DL	<DL	<DL	1.9	1.5	<DL	<DL	<DL	0.7	<DL	<DL	<DL			
Au	ppm	FA430	<DL	<DL	<DL	<DL	0.007	0.173	0.242	0.104	0.019	0.025	0.006	<DL	0.006	<DL	0.02			
Dry density (g/cm3)			2.69	2.54	2.64	2.53	2.63	2.62	2.42	2.19	2.40	2.68	2.72	2.53	2.68	2.58				
Porosity (n)			1.11	1.87	1.13	1.54	1.68	1.65	3.86	7.99	1.99	1.15	1.96	0.48	2.20	3.30				
Magnetic susceptibility (x10 ⁻³ SI Units)			0.614	0.114	5.945	0.007	0.006	0.008	0.217	0.031	0.042	0.002	21.702	0.133	0.034	0.001	0.005			
Hyperspectral Analyses																				
Alunite	%		0.0	0.0	0.0	0.0	0.3	92.1	0.0	0.0	0.0	0.0	0.0	0.0	0.0	0.0	90.4			
Amphibole	%		0.0	0.0	0.0	0.0	0.0	0.0	0.0	0.0	0.0	0.0	0.0	0.0	0.0	0.0	0.0			
Biotite	%		0.0	0.0	0.0	0.0	0.0	0.0	0.0	0.1	0.0	0.0	0.0	0.0	0.0	0.0	0.0			
Chlorite	%		80.4	73.2	71.2	1.4	0.0	0.0	94.7	0.4	0.0	0.0	24.6	30.0	0.1	0.0	0.0			
Dickite	%		0.0	0.1	0.1	0.0	56.5	2.4	0.0	31.7	8.4	3.6	0.0	0.0	0.0	0.7	0.1			
Epidote	%		0.0	9.5	0.0	0.0	0.0	0.0	0.0	0.0	0.0	0.0	0.0	0.0	0.0	0.0	0.0			
Gypsum	%		0.0	0.0	0.0	0.0	0.0	0.0	0.0	0.0	0.0	0.0	0.0	0.0	0.0	0.0	0.0			
Jarosite	%		0.0	0.0	0.0	6.3	0.0	0.0	0.0	0.0	0.0	0.0	0.0	0.0	20.1	0.0	0.0			
Kaolinite	%		0.0	0.0	0.0	0.0	22.7	0.0	0.0	5.4	62.8	64.8	0.0	0.0	0.0	0.0	0.0			
Muscovite	%		0.1	93.5	26.1	94.9	3.6	0.3	95.3	51.8	26.8	18.0	18.0	58.2	75.7	24.3	0.5			
Pyrophyllite	%		0.0	0.1	0.0	0.0	0.0	0.1	0.0	0.3	0.1	1.1	0.0	0.0	0.0	54.2	0.2			
Halloysite	%		0.0	0.0	0.0	0.0	21.5	0.0	0.0	5.0	21.9	1.2	0.0	0.0	0.0	0.7	0.0			
Topaz	%		0.0	0.0	0.0	0.0	0.0	0.3	0.0	0.0	0.0	0.0	0.0	0.0	0.0	91.2	9.2			
Active pixels			58506	98321	58983	67866	110253	42874	69017	63951	95814	94235	66278	60920	90585	130782	57753			
Total Classified pixels			47586	95650	51350	65332	104636	41204	66639	61317	93766	92316	44370	52866	83476	127834	54752			
Classified %			81.3	97.3	87.1	96.3	94.9	96.1	96.6	95.9	97.9	98.0	66.9	86.8	92.2	97.7	94.8			

Abbreviations: aug = augite, plag = plagioclase, HM = Horn Mountain

Kemess North

The alteration zone exposed at the surface at the north-trending Kemess North ridge is hosted by Takla Group basaltic flows and is distinctly zoned from south to north (Figures 5, 6b, and 10a). In the southern parts of the ridge, alteration is characterized by green muscovite with remnants of chlorite (Figure 10g) that gradually transitions northward to a green-grey muscovite-clay (dickite and kaolinite) assemblage (Figure 10e). Further to the north, the proportion of the clays (kaolinite and dickite) increases, forming a whitish colour clay-muscovite assemblage (Figure 10d), which then grades into a zone of pervasive

silicification with white muscovite, kaolinite and dickite that host locally abundant andalusite, corundum, and minor topaz with pyrophyllite (Figure 10b, 10c and 6b). The latter alteration typically shows nodular or patchy textures (Figure 10c). Similarly, silicified and strongly kaolinite- and dickite-altered rocks, with remnants of white muscovite, show characteristic nodular textures of white clay rimmed by quartz (Figure 10d). These alteration textures are similar to the nodular pyrophyllite or patchy silica texture described at the top of porphyry systems (e.g., Longo et al., 2010; Sillitoe, 2010; Hedenquist and

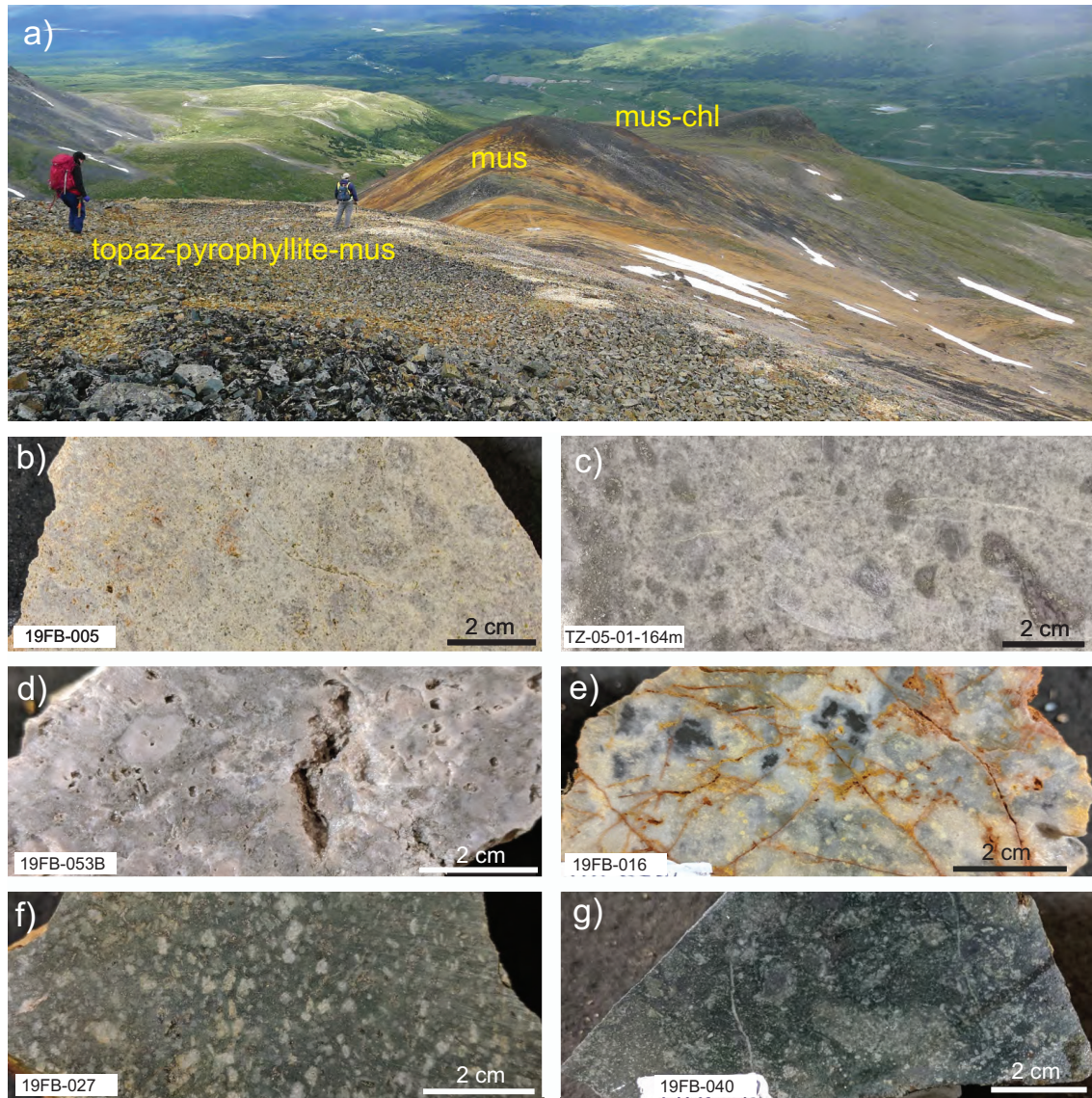


Figure 7: Tanzilla alteration and rock samples: a) looking northeast to the Tanzilla north ridge from the Main zone hill characterized by silicified rock with intense topaz-pyrophyllite-muscovite alteration and limonite-stained volcanic outcrops with muscovite alteration which transitions to muscovite-chlorite; b) plagioclase-phyrific volcanic rock from Tanzilla with pervasive silicification, minor vuggy texture and pale yellow to grey alteration of pyrophyllite, muscovite and topaz; c) sample of a crystal tuff-breccia from a drill hole on the Main zone hill (depth of sample 164 m, along the hole) with pervasive white muscovite alteration, abundant pyrophyllite (confirmed by SWIR), and strong silicification with andalusite, topaz and minor corundum; d) sample of the volcanic rock with silicification, alunite with minor topaz, and white muscovite; e) sample of Tanzilla porphyry with strong silicification and white muscovite alteration with remnants of plagioclase porphyry, cut by jarosite in fractures; f) sample of the host volcanic rock from the margin of the advanced argillic-alteration zone at Tanzilla, with a strong pervasive green muscovite-chlorite alteration; g) sample of volcanic breccia with a distal pervasive chlorite-muscovite alteration. Abbreviations for this and other figures: mus = muscovite, chl = chlorite, epi = epidote

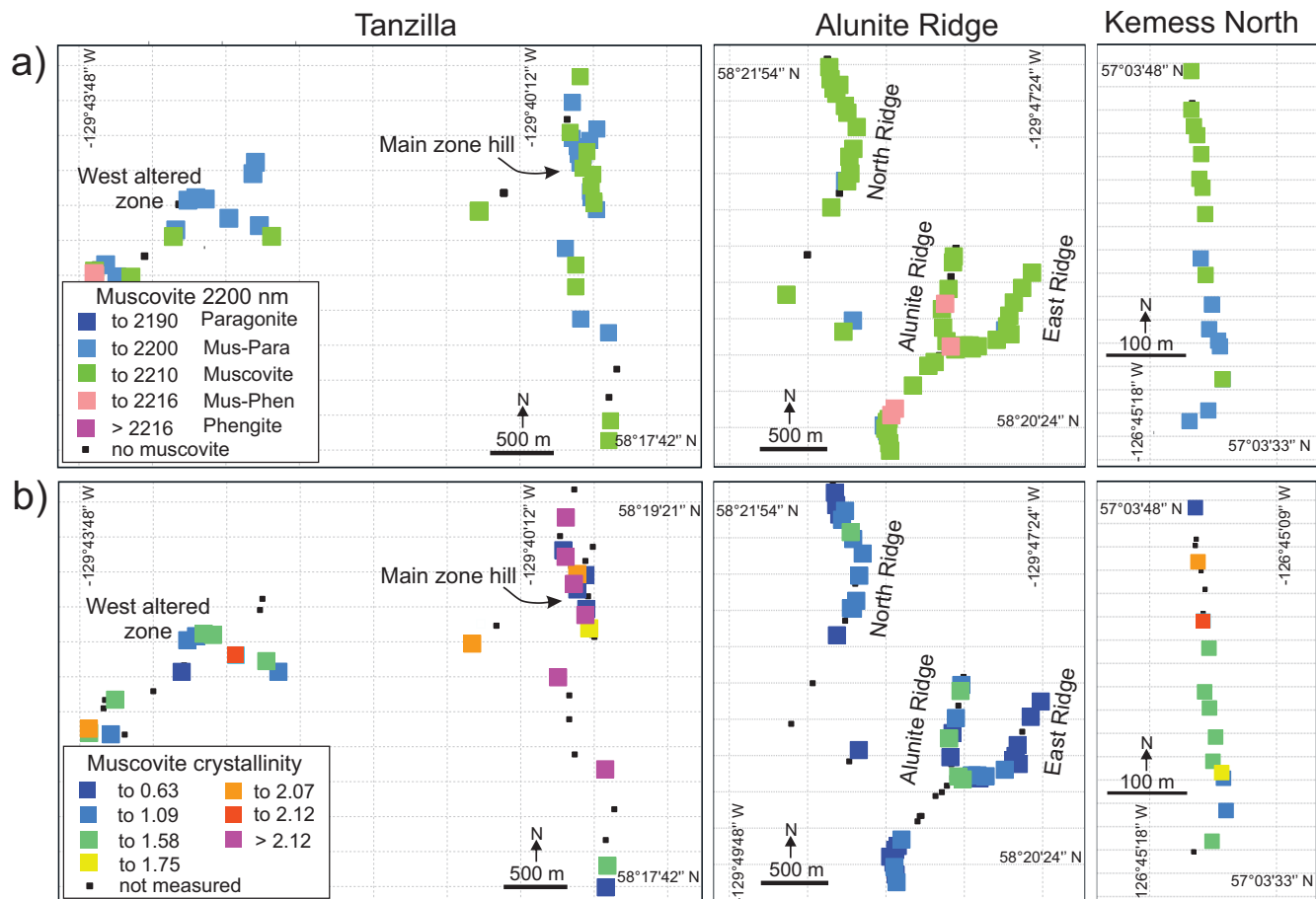


Figure 8: Muscovite alteration identified by hyperspectral SWIR: a) composition of muscovite identified from the position of the 2200 nm wavelength spectral feature; b) crystallinity of the muscovite calculated from the ratio of 2200 nm and 1900 nm wavelength depths of SWIR data. Abbreviations: Para = paragonite, Phen = phengite, Mus = muscovite

Arribas, 2021). Stockwork of quartz veins occurs with the white muscovite-clay alteration (Figure 10f). This strongly advanced argillic-altered Takla rock is in fault contact with the chlorite-epidote-altered volcanic rocks of the Toodogone Formation volcanic rocks to the north. Paragonitic muscovite occurs south of the ridge, whereas K-rich muscovite with higher crystallinity (>1.75) occurs to the north (Figure 8).

Drill core samples from beneath the advanced argillic-alteration have green muscovite-(magnetite-hematite) with disseminated pyrite and chalcopyrite. The chlorite content increases with depth, and the alteration assemblage becomes darker green. Granular quartz veins with chalcopyrite, pyrite, and magnetite (chalcopyrite > pyrite) occur within the green muscovite-chlorite alteration zone. Zones of white muscovite with abundant pyrite locally cut and overprint the green muscovite-chlorite alteration indicating that white muscovite-clay alteration (well developed at shallow levels), overprints the muscovite-chlorite alteration at depth. The chlorite-green muscovite alteration overprints pervasive biotite altered Takla volcanic rock (Figure 10h). These are cut by quartz-magnetite-chalcopyrite-pyrite veins that locally have a pink K-feldspar halo. Both K-feldspar

and muscovite-chlorite alteration zones host copper and gold mineralization at Keness North.

CATHODOLUMINESCENCE OF ADVANCED ARGILLIC ALTERATION MINERALS

Cathodoluminescence (CL) microscopy is a powerful tool that can identify and characterize typical alteration assemblages within ore deposits. In particular, CL studies have characterized multiple generations of quartz in porphyry and epithermal deposits (e.g., Rusk and Reed, 2002; Rusk et al., 2006, 2008; Landtwing et al., 2005; Bennett, 2014; Holley et al., 2017). In this study, luminescence properties of quartz, as well as minerals typically occurring in the advanced argillic altered rocks such as aluminum-rich minerals and clays, were examined. In the suite of samples studied, andalusite typically occurs as a coarse granular phase with dark luminescence, but locally has bodies or fractures with pale green luminescence that may result from an overprint of alteration (Figure 11b), or rarely displays pale green luminescence (Figure 11f). Topaz is fine-grained, resembling quartz (Figure 11a), but has a distinct strong blue luminescence. Corundum occurs as coarse elongated crystals

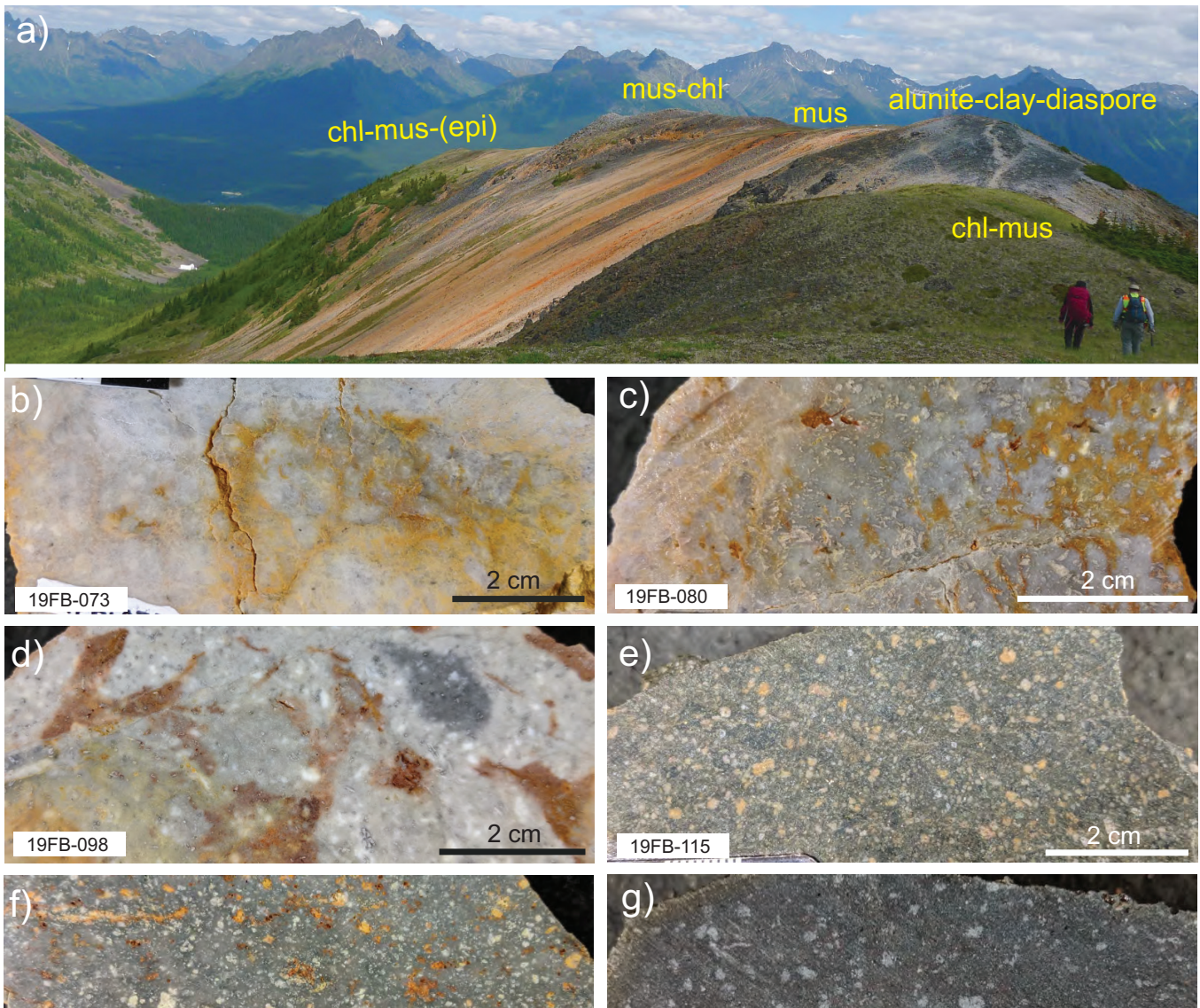


Figure 9: Alunite Ridge host rocks and alteration samples: a) looking northeast along Alunite Ridge showing grey-colour silicified and alunite-clay-diaspore-altered rocks surrounded by muscovite-rich alteration and outboard by limonite stained green muscovite-chlorite alteration and chlorite-muscovite-epidote in more distal locations; b) sample of strongly silicified volcanic rock with dickite-kaolinite and diaspore alteration; c) host volcanic rock with remnants of plagioclase phenocrysts overprinted by silicification and alunite alteration; d) host volcanic rock with remnants of plagioclase phenocrysts overprinted by silicification and grey to white muscovite alteration; e) sample of volcanic rock with pervasive green muscovite-chlorite alteration; f) ample of dark green muscovite-chlorite-epidote alteration; g) sample of host volcanic rock with dominantly chlorite alteration.

with slender (Figure 11d) or granular and fine-grained habits (Figure 11f). Both types of corundum display strong pink luminescence.

Pyrophyllite and clays (kaolinite and dickite), confirmed by SEM quantitative and SWIR analyses, display strong blue luminescence (Figures 11f and h). Andalusite grains are rimmed (Figure 11a) or surrounded by brown and amorphous-looking clays (under plane-polarized light, PPL, Figure 11e) that display pale reddish luminescence (Figure 11f). These are, in turn surrounded by blue luminescent pyrophyllite and clays. Similar textures have been attributed to the alteration of andalusite by pyrophyllite and clays (Watanabe and Hedenquist, 2001). This

is followed by a subsequent retrograde overprint of clays that replaced andalusite rims. It is common to see coarse-grained, blue luminescent clays with stacked platy habits (Figure 11i) with samples containing pyrophyllite or aluminum-rich minerals such as andalusite or diaspore. Dickite, identified by SWIR, is typically present in these samples in addition to kaolinite.

More significant is the occurrence of red luminescent quartz that typically occurs with silicified samples containing variable amounts of the blue luminescent clays, pyrophyllite, or muscovite. The red luminescent quartz can be coarse-grained and contain bodies of blue luminescent clays (Figures 12a and b), or fine-grained and intergrown with clays (Figures

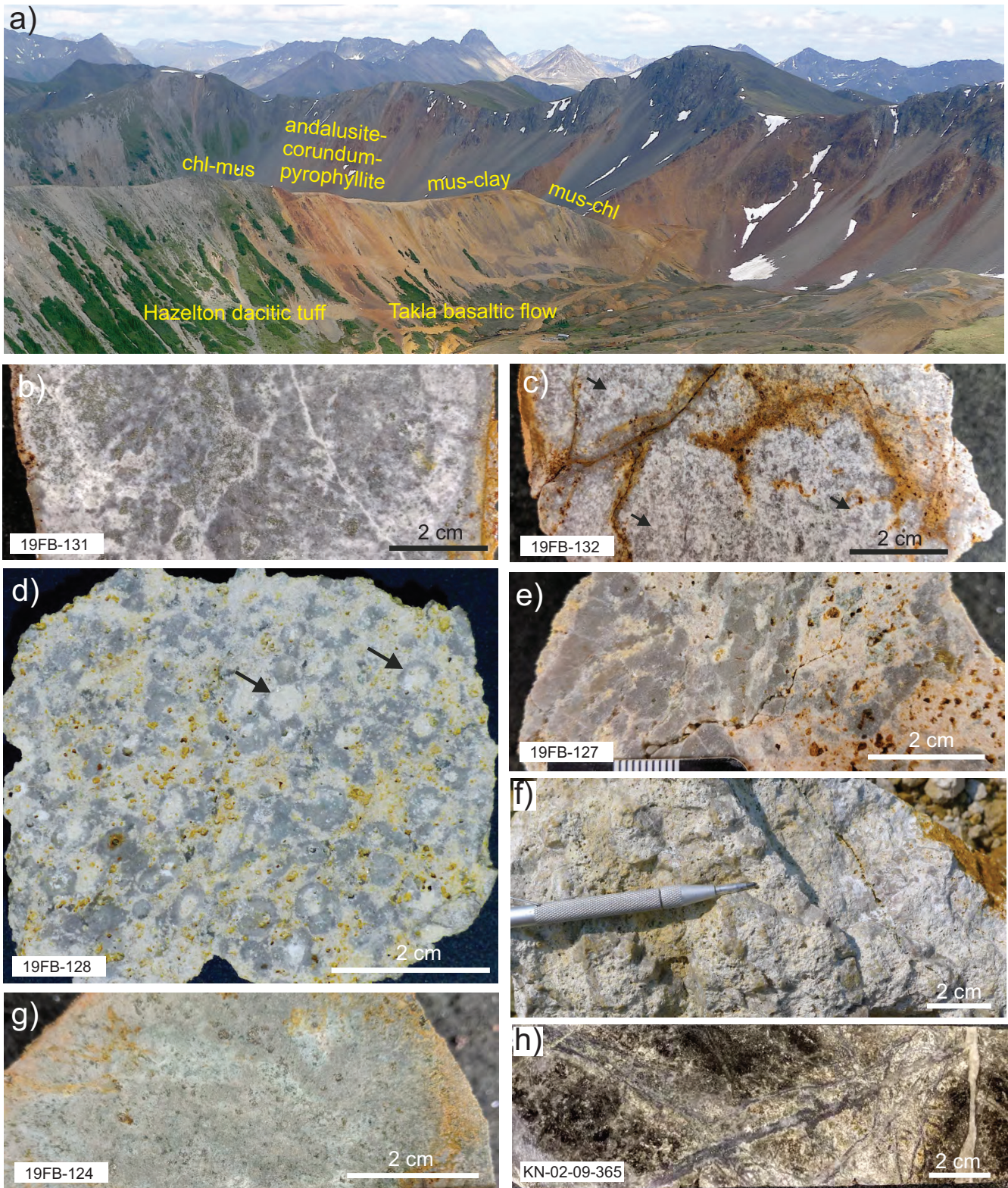


Figure 10: Kemess North host rock and alteration samples: a) looking southeast to the Kemess North ridge showing strongly altered Takla Group volcanic rocks with orange gossan coloration displaying distinct alteration assemblages in probable fault contact with the Hazelton Group volcanic rocks; b) strongly silicified Takla volcanic rock with disseminated pyrite and abundant andalusite and corundum with bodies of white alteration of muscovite with kaolinite and dickite; c) Takla volcanic rock with silicification, kaolinite, dickite, white muscovite alteration, pyrophyllite, and andalusite. Note the nodular texture of the alteration (shown by arrows); d) strongly kaolinite-dickite-altered Takla volcanic rock with remnants of pyrophyllite and strong silicification, showing characteristic white, nodular clay texture rimmed by quartz (shown by arrow); e) Takla volcanic rock with silicification, muscovite, dickite, and kaolinite alteration; f) Takla volcanic rock with white muscovite, kaolinite and dickite alteration cut by stockwork of quartz veins; g) Takla volcanic rock with pale-green muscovite-(chlorite) assemblage; h) Takla volcanic rock with strong, pervasive, biotite alteration overprinted by chlorite, green and white muscovite, and cut by quartz-magnetite-pyrite-chalcopyrite veins. Sample from drill hole KN-02-09 at 365 m down hole.

12c and d). Quartz occurring more distally with muscovite-chlorite alteration does not show luminescence. Moreover, cathodoluminescence imaging identifies a younger generation of quartz, which cuts the red luminescent quartz but lacks a luminescence response (dark; Figure 12f). Coarse euhedral quartz veins that occur with alteration in Quartz Lake low-to-intermediate sulphidation type mineralization, south of Alunite Ridge (Figure 4), typically display yellow luminescence consistent with late quartz in vuggy silica described by Holley et al. (2017). These quartz veins are also cut by a late quartz that lacks luminescence (Figures 12g and h). The late quartz looks similar to the older generation quartz in hand sample and under a petrographic microscope and can only be distinguished from the latter by the difference in luminescence (Figures 12e and g).

These limited observations suggest that the red luminescent quartz, particularly when occurring with blue luminescent clays, has formed in a central setting, probably at a higher temperature, relative to those of with the subsequent, probably lower temperature, quartz that does not display luminescence.

HOST ROCK COMPOSITION AND EFFECT ON ALTERATION

Host rock composition affects the type and intensity of alteration assemblages. Therefore, it is important to characterize host rocks and their influence on alteration (Figure 13 and 14) in order to confidently determine alteration-related vectors. Data from available geological maps and field observations have been used to classify rock types. Geochemical trace-element data can also characterize the host rocks following the methods described by Halley (2020). A V-Sc scatterplot distinguishes volcanic rocks of the Takla Group from those of the Hazelton Group (Figure 13a). Both V³⁺ and Sc³⁺ have similar behaviour and substitute for Fe in amphibole, pyroxene, and biotite during crystallization (Li and Lee, 2004; Halley, 2020). All host rocks have positive trends of Sc against V (Figure 13a); however, the slopes typically vary slightly for different units. The Takla Group data show the least amount of slope change with increasing V compared to the Toodoggone Formation rocks, which display the highest slope of the trendline. The Horn Mountain Formation rocks plot between the other two units.

The Th-Sc relationships can characterize the mafic vs. felsic composition of the host rocks. The Th-Sc diagram (Figure 13b) shows that all rock units have similar Sc values, except for some Takla samples that display the highest Sc values; higher Sc content means a more mafic rock composition (Halley, 2020). There is a weak negative correlation between Sc and Th values, especially for Takla Group and Toodoggone Formation rocks. However, the Th content shows some distinct variations. Takla Group volcanic rocks, relative to Hazelton Group rocks

(Toodoggone and Horn Mountain formations), have lower Th concentrations. Within the Hazelton Group, the Horn Mountain Formation has the largest degree of scattering and reaching the highest Th values. The Sc concentration corresponds to high-Fe rocks, and Th, an incompatible element, stays in the melts and incorporates into late-stage crystallizing mineral phases (Pearce and Norry, 1979). Therefore, the trend from high Sc to high Th reflects a change in composition from more mafic Takla volcanic rocks to mafic-intermediate felsic rocks of the Toodoggone and Horn Mountain formations.

When attributed for alteration assemblage (Figure 13c), distinct host rock influences on alteration distributions are not apparent. Although rocks with higher Th (≥ 8 ppm) do not show signs of chlorite-dominated alteration, they do exhibit biotite and muscovite-chlorite alteration. Therefore, it is possible that more felsic rocks of the Hazelton Group rocks are weakly impacted by chlorite-type alteration, but the available data suggest that this was not significant.

A V/Sc versus Sc diagram can also discriminate between rock types (Halley, 2020) and determine if the alteration intensity has influenced these trace elements abundance (Figures 13 and 14). A slight decrease in V/Sc ratios in all rock units is associated with a lower Sc content (Figure 13d) that corresponds with higher SiO₂. Decreasing V is attributed to the fractional crystallization of magnetite, which incorporates V (Halley, 2020). A similar diagram, but attributed for the intensity of alteration (Figure 13e), shows that host rocks have no distinct control on alteration intensity and that alteration varies from weak to very strong occur in all rock units. The alteration intensities were quantified from weak to strong on the basis of field and macroscopic hand sample characterization. However, there is an increase in the V/Sc ratio at lower Sc concentrations. A high V/Sc ratio has been used to indicate early crystallization of hornblende and clinopyroxene in fertile hydrous magmas (Loucks, 2014). Given the limited number of samples, it is difficult to argue that some of the host rocks in the study area had originated from more fertile magmas. Comparing the values from Figure 13d with those representing the intensity of alteration (Figure 13e), it appears that in this dataset, the high V/Sc values may result from intense advanced argillic alteration, especially intense muscovite and silicification. Therefore, it is possible that strong alteration in advanced argillic-altered rocks can increase the V/Sc ratio of the rock.

ALTERATION COMPOSITIONAL VECTORS

Hydrothermal alteration results in chemical and mineralogical changes in a rock (Meyer and Hemley, 1967). The mineralogical changes, which form a zoned pattern around the porphyry copper deposits, have been used successfully in exploration vectoring (e.g., Sillitoe, 2010). These mineralogical changes

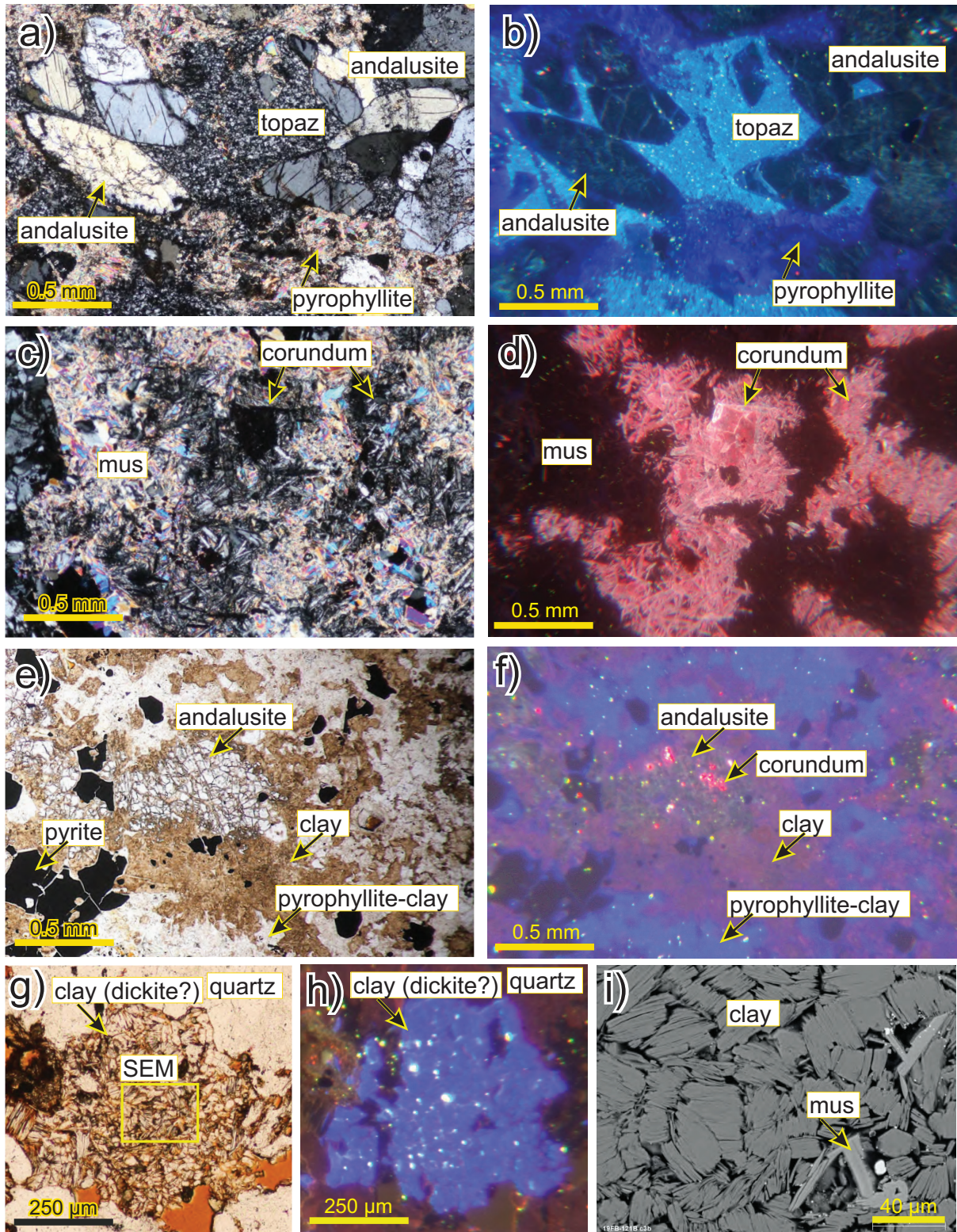


Figure 11: Cathodoluminescence petrography of samples with aluminum-rich alteration: a) image in cross-polarized light (XPL); and b) same field of view but with cathodoluminescence (CL) depicting coarse andalusite grains, locally with green luminescence, in a groundmass of fine-grained topaz with blue luminescence and pyrophyllite with dark blue luminescence (sample TZ-15-01-164 from Tanzilla drill hole); c) and d) XPL and CL images, respectively, showing a cluster of corundum crystals with distinct pink luminescence and elongated slender prism habit surround by and intergrown with coarse crystals of muscovite (sample 19FB-131 from Kemess North); e and f) plane-polarized light (PPL) and CL images, respectively, showing andalusite grains with pale greenish luminescence surrounded by red luminescent clay (kaolinite and/or dickite), which has a brown colour in PPL, and in turn surrounded by blue luminescent pyrophyllite and clays. This zoning may suggest alteration of pyrophyllite to clays and then to andalusite (sample 19FB-131 from Kemess North); g and h) PPL and CL images, respectively, of a body of medium to coarse-grained blue luminescent clay surrounded by red luminescent quartz (sample 19FB-121B from Kemess North); i) scanning electron microscope (SEM) image of the clay in Figure 11g and h (see inset) showing the platy aggregate (books) of dickite or kaolinite (both identified by SWIR) with remnants of muscovite.

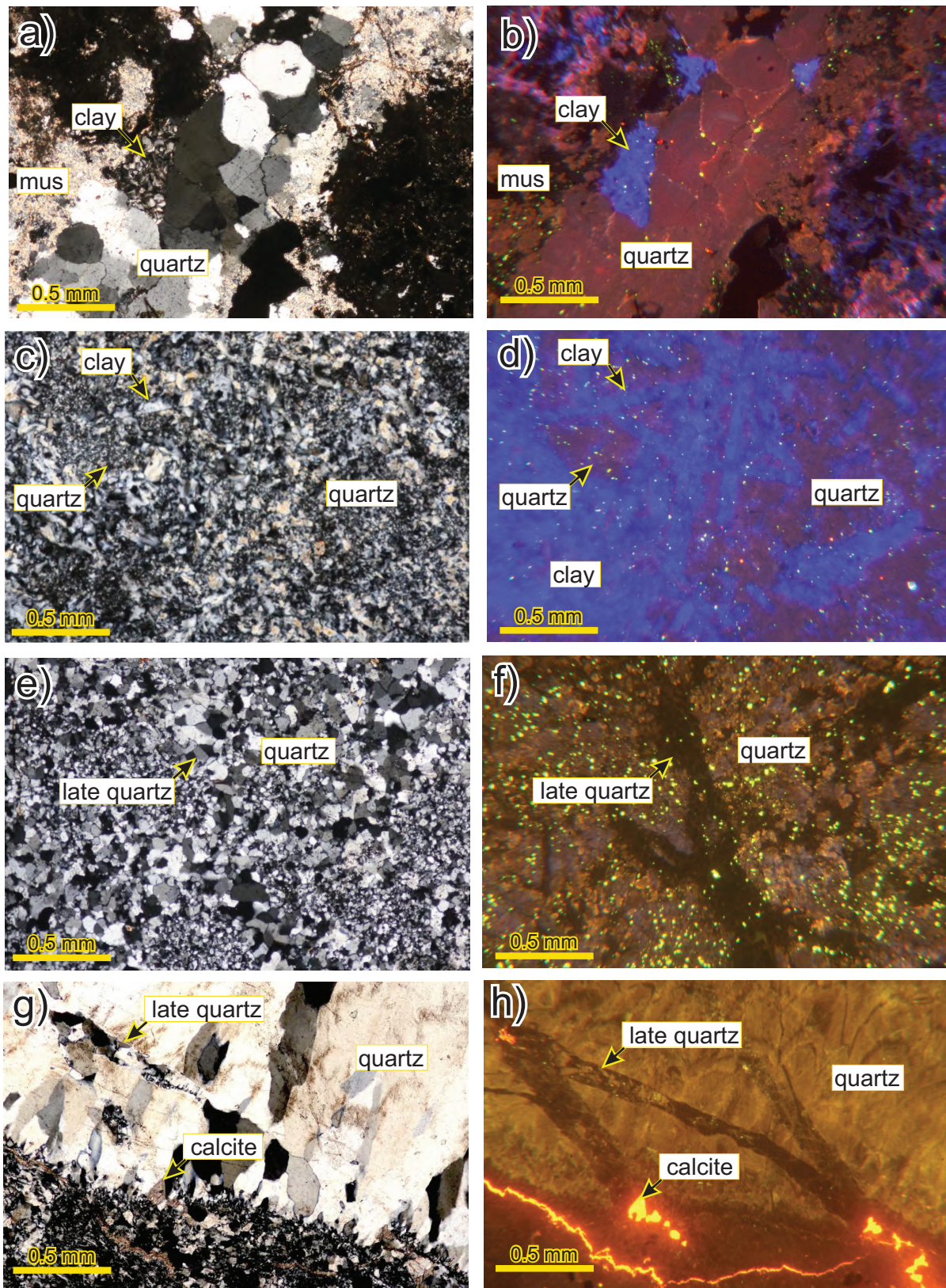


Figure 12: Cathodoluminescence of quartz in advanced argillic altered rocks: a and b) XPL and CL images of quartz of advanced argillic alteration with distinct red luminescence, intergrown with blue luminescent clay and some muscovite (sample 19FB-121B from Kemess North); c and d) XPL and CL images of red luminescent quartz intergrown with blue luminescent clay (dickite/kaolinite). Note that clays have formed disseminated and tabular vein-shaped bodies (sample 19FB-073 from Alunite Ridge); e and f) XPL and CL images of fine-grained disseminated quartz with red to brown luminescence, locally showing pale blue luminescence due to mixture with clays, cut by a probably later stage quartz vein (labeled as late quartz), which shows no luminescence. Note that types of quartz are not identifiable in XPL images. The abundant fine-grained green luminescent grains are from polishing materials that filled the vuggy texture of the rock (sample 19FB-006 from Tanzilla).

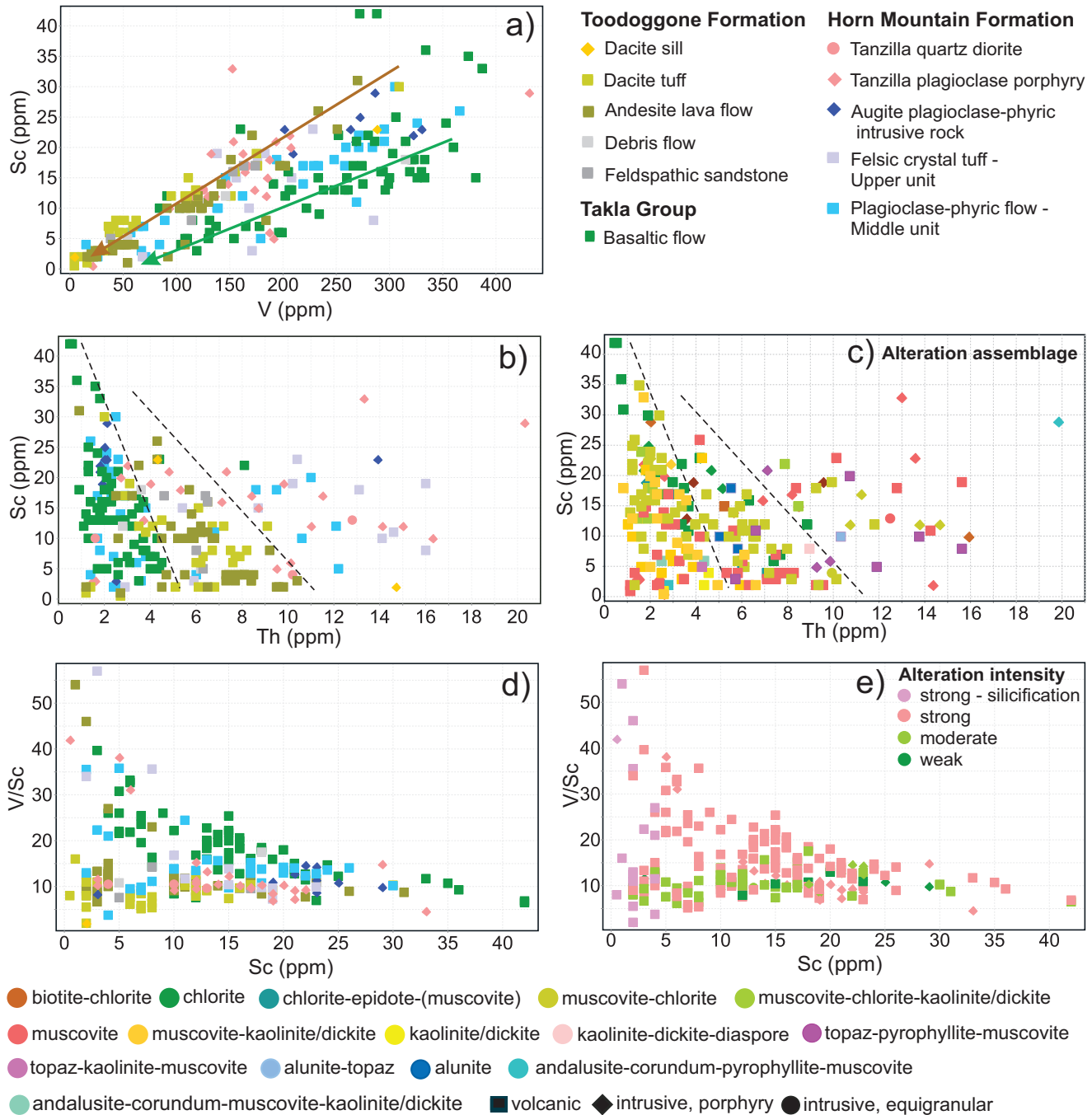


Figure 13: Scatterplots used to distinguish rocks of the Takla Group from those of the Hazelton Group in the study areas: a) V versus Sc diagram showing host rock composition (arrowed lines show the main compositional trends); b) Th versus Sc scatterplot showing host rock composition (dashed lines separate the main compositional changes); c) the same diagram as in (b) but colour-coded by alteration assemblages; d) V/Sc versus Sc scatterplot showing host rock composition; e) the same diagram as in (d) but colour-coded by alteration intensity which was defined visually.

commonly correspond to distinct whole-rock chemical changes. Previous researchers have evaluated the application of whole-rock geochemical data to identify and map alteration footprints (e.g., Stanley and Madeisky, 1996; Large et al., 2001; Williams and Davidson, 2004; Davies and Whitehead, 2006; and more recently Escolme et al., 2019; Halley, 2020; Barker et al., 2021). This provides a complement to the traditional field and alteration mineral mapping (latter assisted by SWIR and XRD)

and provides vectors using subtle chemical changes that may occur in a single mineral phase.

Alkali-Alumina Diagram

Muscovite and various types of clay minerals such as kaolinite and dickite typically characterize alteration assemblages at shallow levels of porphyry deposits. Field observations indicate a zonation from distal green muscovite-chlorite to pale-

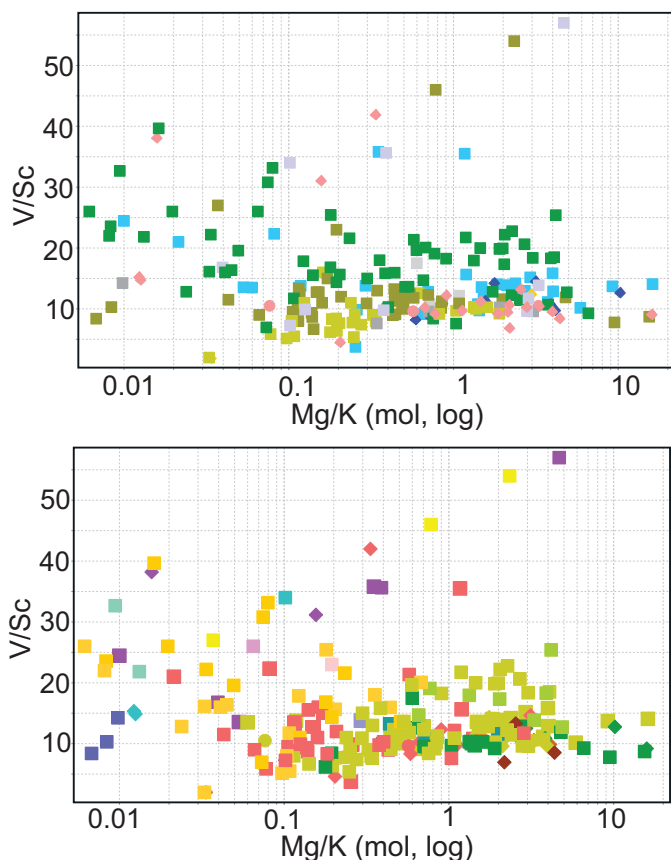


Figure 14: Scatterplots showing effects of host rock on Mg/K molar ratio: a) V/Sc versus Mg/K scatterplot showing host rock composition; b) the same diagram as in (a) but colour-coded by alteration types. For colour symbols, see Figure 13.

green muscovite and white muscovite-clay (kaolinite, dickite) assemblages proximal to the top of a porphyry deposit and central parts of advanced argillic alteration zones (Figure 6b). The alkali-alumina diagram of Davies and Whitehead (2006) has been widely used to map K-feldspar and muscovite alteration minerals (Halley, 2020) using the molar ratio of Na and K to Al. The data show a trend of compositional change from high Na/Al towards higher K/Al, which probably reflects an earlier sodic alteration (e.g., albite) was overprinted by K-silicate (e.g., biotite and/or K-feldspar) and/or phyllic (e.g., muscovite) alteration events. This trend largely corresponds to samples with chlorite, locally with remnants of biotite, muscovite-chlorite and muscovite alteration assemblages. A cluster of samples occurs at distinctly low Na/Al with K/Al values form an array from the muscovite node to kaolinite node, reflecting a decrease in muscovite abundance. This cluster, is largely dominated by samples characterized by muscovite, muscovite mixed with clays (kaolinite, dickite), pyrophyllite, andalusite, corundum, diaspore, topaz, and alunite corresponding to more intense phyllic-advanced argillic alteration assemblages.

K-Mg-Alumina Diagram

The Davies and Whitehead (2006) alkali-alumina diagram compares Na and K variations and so is mainly sensitive to feldspar composition and assumes that muscovite formed primarily after feldspar. This assumption holds in felsic, feldspar-rich rocks lacking mafic minerals, but in more mafic rocks muscovite forms after mafic minerals. Amphibole may alter to biotite, for example, during the K-silicate alteration. Biotite or amphibole then alters to chlorite and muscovite during the overprinting phyllic alteration. Therefore, in these host rocks, changes in the composition of the rock, particularly, Mg or Fe, K, and Al, as a result of mafic mineral alteration can provide better vectors for alteration.

We introduce a new discrimination diagram based on the molar ratio of Mg/K and K/Al which better map phyllic and advanced argillic alterations in andesite and basaltic andesite host rocks. The introduction of Mg incorporates the influence of chlorite and the precursor amphiboles and biotite to the chemical changes from host rock alteration. As a result, this diagram better discriminates the alteration assemblage from whole rock geochemical data (Figure 15b).

To predict the alteration mineralogy using whole-rock geochemical data, the K-Mg-alumina diagram is divided into zones for grouping simplified alteration assemblages (Figure 15c). The green muscovite-chlorite alteration assemblage corresponds to a Mg/K decrease with increasing K/Al that indicates an evolution towards a composition between pure K-feldspar and biotite. This suggests the existence of an earlier K-silicate alteration whose remnants are now locally preserved as pervasive biotite alteration partly altered to chlorite (e.g., Figure 10h). Thus, samples of muscovite with K/Al (mol) > 0.33 suggest the occurrence of precursor biotite in the rock. The overprinting phyllic alteration formed the pale-green muscovite with a quartz mineral assemblage. Muscovite of this alteration type occurs in a cluster near phengite composition and towards the K-rich muscovite composition. White muscovite-clay, clay, pyrophyllite, topaz, andalusite, corundum, diaspore, and alunite occur at low Mg/K and low K/Al, towards kaolinite composition. These minerals form due to significantly stronger H⁺ metasomatism, which results in the formation of Al-rich minerals at the expense of both K and Mg depletion.

The correlation of field and SWIR mineralogy with the geochemical data plotted on the K-Mg-alumina diagram defines four fields, each corresponding approximately to an alteration assemblage (Figure 15c). To correlate and compare this geochemical classification with the actual alteration mineralogy, the data are plotted on the surface map (Figure 6c). This shows the chemical classification identifies the main alteration zones well and, in particular, characterizes the zoning from green muscovite-chlorite to pale-green muscovite

and white muscovite, clay-rich advanced argillic alteration zones. Therefore, the K-Mg-Al diagram can be an effective tool to distinguish and map chlorite, muscovite and clay alteration assemblages from geochemical data, particularly in intermediate to mafic volcanic host rocks.

Advanced Argillic Alteration by K/Rb-Alumina Diagram

Minerals that commonly occur in the advanced argillic alteration zone include pyrophyllite, kaolinite, dickite, alunite, topaz, andalusite, diaspore, and corundum, in addition to quartz. Most of these minerals are dominated by Al and Si, but

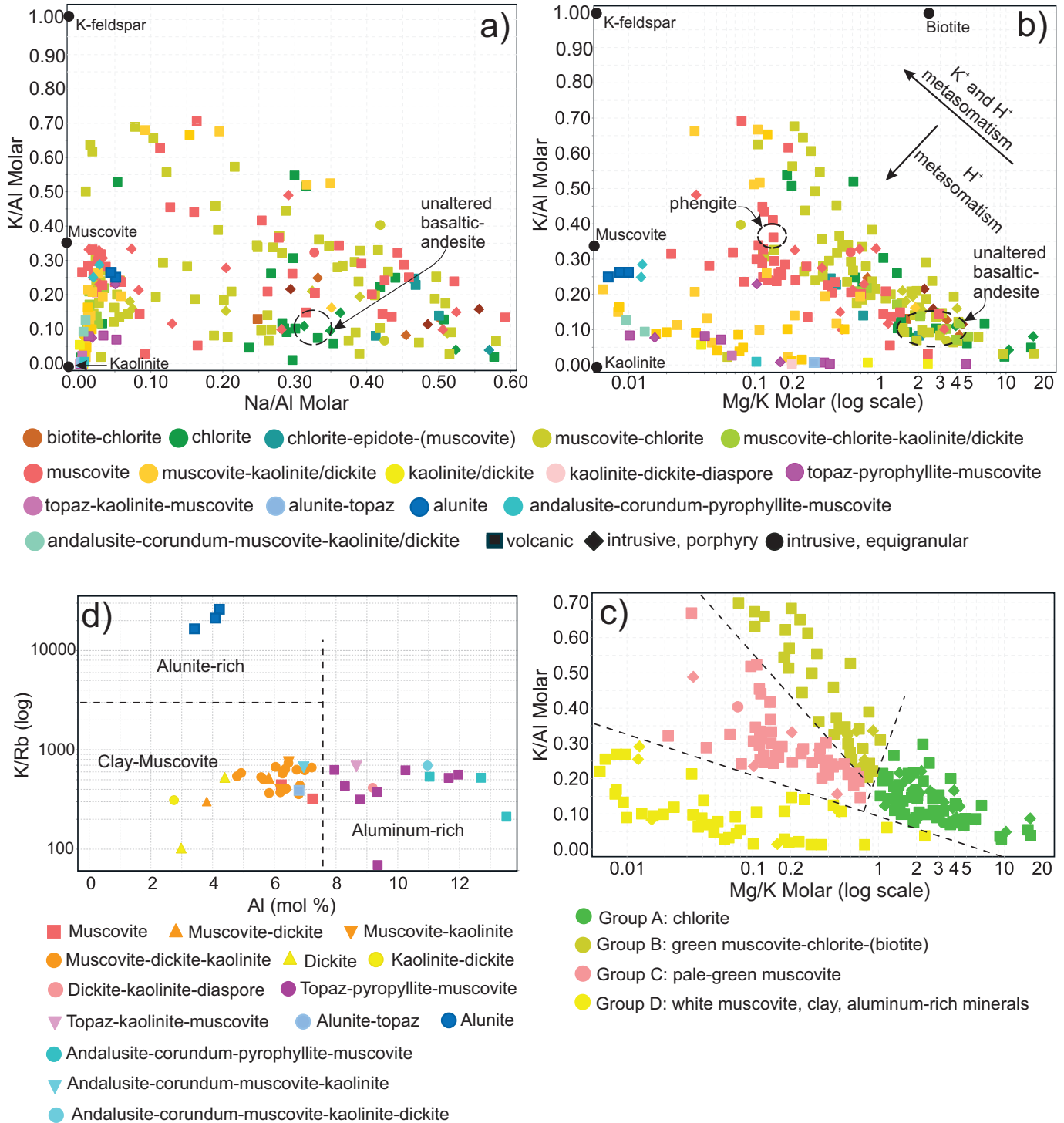


Figure 15: a) Alkali-alumina diagram (Davies and Whitehead (2006)) showing composition of alteration assemblages; b) K-Mg-Al diagram showing the composition of alteration assemblages; c) K-Mg-Al diagram with the same sample dataset as in (b) used to divide the space into main alteration groups; d) K/Rb-alumina diagram for identification of samples with Al-rich and alunite phases.

some such as diaspore and corundum even lack Si (alunite has K and S, and topaz has F). Given the abundance of quartz in the zones of advanced argillic alteration, Al is the only element that can be used to geochemically identify most of the mineral assemblages. Aluminum in these rocks is interpreted to be residual concentrated in the form of aluminum-rich minerals as a result of removal of most of the other elements during the advanced argillic alteration. Ideally, we would like to be able to define zones of alteration with andalusite, diaspore, topaz, and corundum or alunite from the dominant quartz, clay, and muscovite alterations and distinguish them from the dominant quartz, clay, and muscovite alterations. This could provide a vector towards more central parts of the system that potentially occur above porphyry copper mineralization.

Considering the importance of Al in advanced argillic alteration, the Al composition in minerals are important: corundum has the highest Al (40% molar); andalusite and diaspore each have 25% molar Al; topaz has 20.2% compared to kaolinite at 11.8%, and muscovite has 14.14% molar Al. Alunite has similar Al to kaolinite (11.5% molar) but also has high (51.7%) volatile (H₂O and SO₃) concentrations. Al-rich phases such as andalusite and diaspore are challenging to identify in the field, especially when they are fine-grained. Pyrophyllite resembles muscovite even in a thin section, and andalusite and corundum are not typically identifiable by SWIR analyses.

The concentration of aluminum (on a molar basis) can be simply used to identify the aluminum-rich phases in a geochemical dataset. Alunite can be distinguished by its high K/Rb ratio because rubidium readily substitutes for potassium in most silicate minerals, but it does not substitute for potassium in sulfate minerals such as alunite (Halley, 2020). Therefore, a diagram using Al (molar%) against K/Rb can potentially distinguish most Al-rich minerals and alunite of the advanced argillic alteration from the commonly widespread muscovite and clay alteration assemblages using whole-rock geochemical data.

The application of the K/Rb-Al diagram has been tested on the geochemical data from this study (Figure 15d). To do this, group D on the K-Mg-alumina diagram (Figure 15c), which includes minerals of the advanced argillic alteration assemblage, is plotted on the K/Rb-alumina diagram (Figure 15d). Samples are colour-coded in Figure 15d by the mineral types identified by SWIR and petrography. All samples with corundum, andalusite, topaz, or pyrophyllite-topaz plot at >7.5% molar Al. Alunite-rich samples plot above the 3000 K/Rb line. Therefore, we propose that K/Rb-alumina diagram can help to identify alunite and aluminum-rich phases and zones with intense advanced argillic alteration and provide a vector for zones of more intense H⁺ metasomatism and potentially central parts of the advanced argillic alteration zone.

GEOCHEMICAL VECTORS

Trace-element geochemical data of various metals can be used in the advanced argillic alteration environment to indicate proximity to porphyry copper mineralization. Copper is not present in notable concentrations in advanced argillic altered rocks of the study areas and may have been depleted (<100 ppm) within the zones of intense advanced argillic alteration relative to the rocks associated with distal muscovite-chlorite alteration (Figures 6b, 16a). Supergene oxidation, as evident by partial oxidation of pyrite to jarosite, may have further leached any near-surface copper. Gold locally shows weak anomalies (~0.1 ppm) in advanced argillic altered rocks at Tanzilla and Alunite Ridge, but the data do not reveal a clear trend (Figure 16b). At Kemess North, there are higher concentrations of Au within the muscovite-chlorite-altered rocks in the southern parts of the ridge, whereas Au values are < 0.1 ppm in the muscovite-clay-altered rocks on the northern side of the ridge (Figure 16b). Arsenic concentrations occur with the advanced argillic alteration at Alunite Ridge (23–236 ppm) and Tanzilla (14–23 ppm), whereas the As concentration at Kemess North is low (<2 ppm; Figure 16c). Zinc is primarily depleted from the zone of advanced argillic alteration at Tanzilla and the zone of intense muscovite-clay alteration at Kemess North (<30 ppm). At Alunite Ridge, high zinc concentrations (>700 ppm) occur in the East Ridge, distal to the main area of Alunite Ridge (Figure 16d).

MDRU Porphyry Index (MPIx)

Similar to the mineral zoning, trace metals in porphyry deposits are zoned upward and outward from the copper mineralized (>0.1 wt.% Cu) zone in the general sequence Mo, W, Sn, Se, Te, Bi, Sb, As, Li, and Tl (Halley et al., 2015). Whereas the concentration of metals can provide evidence of a mineralized system, the applicability of their variations and use in vectoring is affected by the intensity of mineralization and level of exposure. Therefore, a ratio of the sum of selected elements can provide a more robust vectoring indicator tool for mineralization. The MDRU Porphyry Index (MPIx; Bouzari et al., 2020) compares the relative proportion of elements occurring at deeper levels of porphyry deposits (Cu, Mo, Sn, W) to those occurring at shallower levels (Sb, As, Ag, Tl, Li). Element concentrations were normalized by multiplying by a factor (>1 or <1) such that all the elements have approximately a similar effect on the ratio. A higher MPIx number indicates closer proximity to porphyry-type mineralization.

$$\text{MPIx} = \frac{\frac{\text{Cu}}{10} + \text{Mo} + (10 \times \text{W}) + (20 \times \text{Sn})}{(5 \times \text{Sb}) + (20 \times \text{Tl}) + \text{Ag} + \text{As} + \text{Li}}$$

Application of this index to the current study (Figure 17a) shows that, on a vertical profile, Kemess North has the highest MPIx

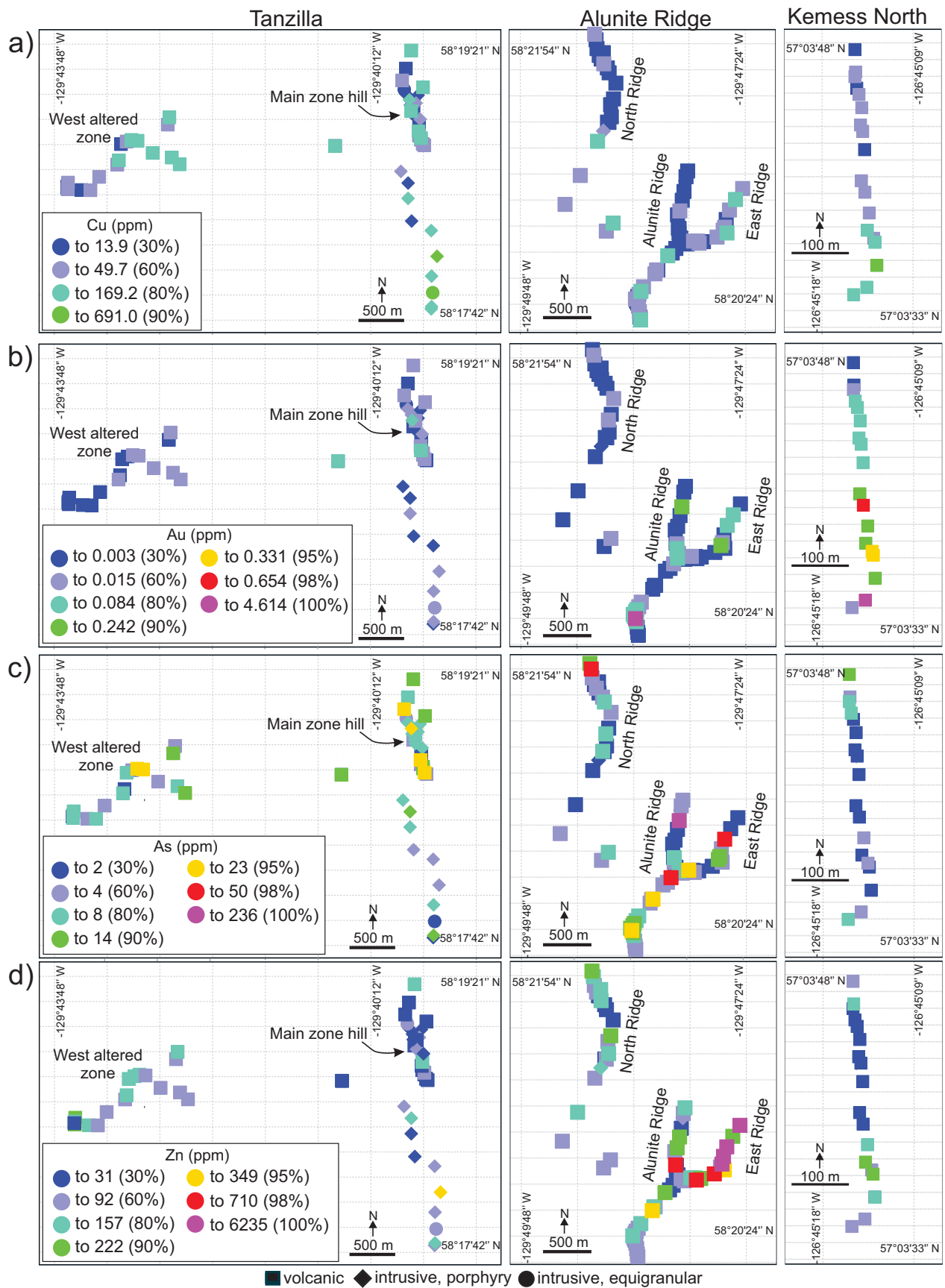


Figure 16: Trace-element distribution in the Tanzilla, Alunite Ridge, and Kemess North mineral properties, showing: a) Cu; b) Au; c) As; d) Zn.

values and therefore represents a deeper level of alteration relative to Tanzilla or to Alunite Ridge that shows the shallowest geochemical signatures. The MPIx ratio vectors toward the zones of intense central alteration, especially toward the northern side of the ridge at Kemess North and toward the hill in the Tanzilla Main zone. At Alunite Ridge, the MPIx indicates the main central parts of the alteration, but the vectoring signature is weak and dominated by low MPIx values.

MDRU Porphyry Index-Lateral (MPIx-Lateral)

MPIx provides a tool to map the vertical proximity and vector in porphyry copper systems. However, at very shallow levels, especially within areas of strong advanced argillic alteration, elements such as Cu, Mo, W, and Sn typically have low concentrations (Halley et al., 2015) over much of the altered area and the resulting MPIx value may not provide a lateral vector toward the top-central parts of the porphyry system. To complement the MPIx, the MDRU Porphyry Index-Lateral (MPIx-Lateral) is introduced, which compares metals that are enriched in the shallow parts of a porphyry system (Sb, As, Tl) relative to those that are more laterally dispersed (Halley et al., 2015) and typically have higher concentrations in more distal parts of the porphyry system (Zn, Mn). Element concentrations are multiplied or divided by an appropriate factor for normalization:

$$\text{MPIx-Lateral} = \frac{(5 \times Sb) + (20 \times Tl) + As}{\frac{Zn}{10} + \frac{Mn}{50}}$$

The MPIx-Lateral (Figure 17b) maps the advanced argillic alteration at the hill in the Tanzilla Main zone, where its footprint shows gradually decreasing values to the east and south. It also shows the Alunite Ridge central zone with decreasing values toward North Ridge. At Kemess North, the MPIx-Lateral values are weaker, given its deeper setting and smaller sampling interval relative to Tanzilla and Alunite Ridge but still vector toward the more intensely altered parts of the ridge.

Na-Ca Depletion Index

Zones of advanced argillic alteration are characterized by intense removal of many rock-forming elements, mainly Ca and alkali metals such as K and Na, due to cooling and leaching of the host rock by low-pH fluids (Meyer and Hemley, 1967; Hedenquist and Arribas, 2021). Therefore, zones of advanced argillic alteration and areas with the highest intensity of alteration will be characterized by mobile elemental loss. Potassium is usually fixed with the formation of pervasive muscovite alteration but Ca and Na depletion, in most cases, correlate with the intensity of alteration.

In order to estimate and quantify the Ca and Na loss, the concentration of Ca and Na are typically compared with an immobile element. Aluminum, and high field strength elements

(HFSE) such as Zr, Ti, and Nb are commonly considered the most immobile elements during an open-system alteration in many settings (e.g., Ague and van Haren, 1996; Booden et al., 2011). Although many studies have shown some mobility for these elements, particularly at very high temperatures or at pH <2.5 (e.g., Jiang et al., 2005, and references therein). Figure 18, in which samples are colour coded by alteration types, compares the concentration of Na+Ca with reference to Al, Zr, Ti, and heavy rare earth elements (HREE) concentrations. The Al concentration for most samples is between 7 to 10% regardless of Na+Ca concentration (Figure 18a). The exceptions are samples with very low Na+Ca concentrations (<1%), which are typically characterized by strong aluminous alteration (topaz, corundum, andalusite with Al>12%) or muscovite-clay with strong silicification (Al<5%). This relationship suggests that for most altered samples, the Al probably remained immobile during the alteration, and the Na+Ca depletion was probably compensated by the addition of K of the muscovite alteration. At the very low pH environment where all alkali elements are leached, the residual Al causes a scatter of Al concentration given the closure (constant sum) effect of the geochemical data (e.g., Ague and van Haren, 1996). But, locally, Al mobility cannot be ruled out, resulting in, for example, andalusite or topaz-rich bodies. Subsequent, silicification will cause further scatter of the Al. Zr, Ti, and HREE show similar relationships but with slightly more scatter of data relative to Al (Figure 18b, c, and d).

Therefore, in this dataset, Al is selected as a reasonable immobile element to quantify the Na+Ca depletion but we have taken a conservative approach and eliminated a few samples that have Al concentration >12% or <5% for the calculation of the depletion index (these samples are shown by light grey colour in the maps, Figure 17c). The following elemental ratio is suggested to map the Na-Ca depletion (all in percent):

$$\text{Na-Ca depletion index} = \frac{Al}{Na + Ca}$$

The application of the Na-Ca depletion index to the study sites shows that the zones of advanced argillic alteration have the greatest Na and Ca depletion, with the index gradually decreasing distally (Figure 17c). At Kemess North, where muscovite-dickite-kaolinite alteration is dominant, the Na and Ca depletion is less intense compared to the advanced argillic alteration at Tanzilla and Alunite Ridge but still vectors, with increasing Na-Ca depletion northward, toward the zone of intense muscovite-dickite-kaolinite alteration.

ROCK PHYSICAL PROPERTY VECTORS

Hydrothermal alteration changes the mineralogical and chemical composition of the host rocks, which also changes the physical properties of the rock, such as its magnetic susceptibility, density, and porosity. Therefore, if the mineral

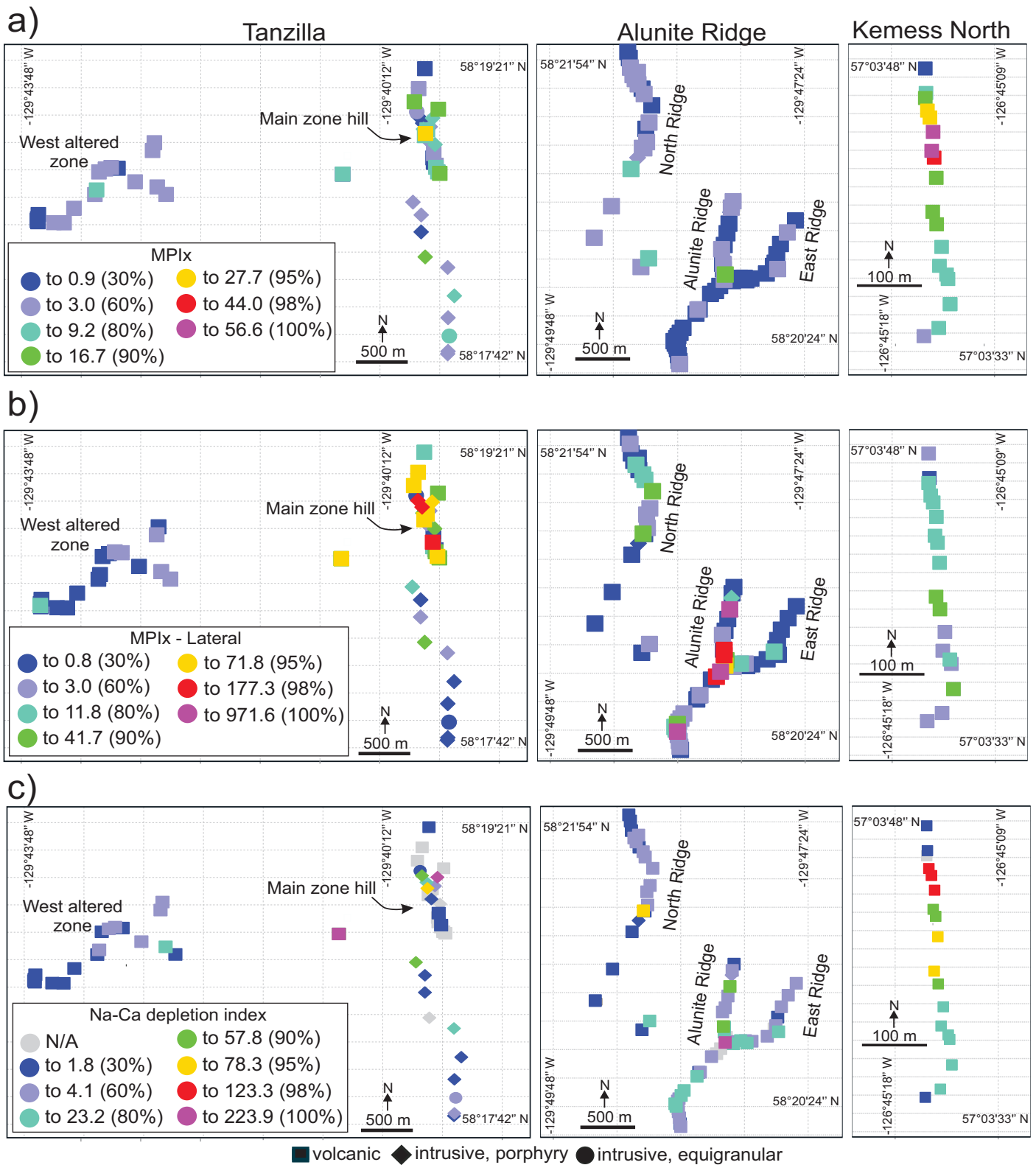


Figure 17: Distribution of the relative proportion of elements (samples colour-coded) occurring at various levels of porphyry deposits at the Tanzilla, Alunite Ridge, and Kemess North study areas determined using: a) the MDRU Porphyry Index (MPIx); b) the MDRU Porphyry Index-Lateral (MPIx-Lateral); c) the Na-Ca depletion index.

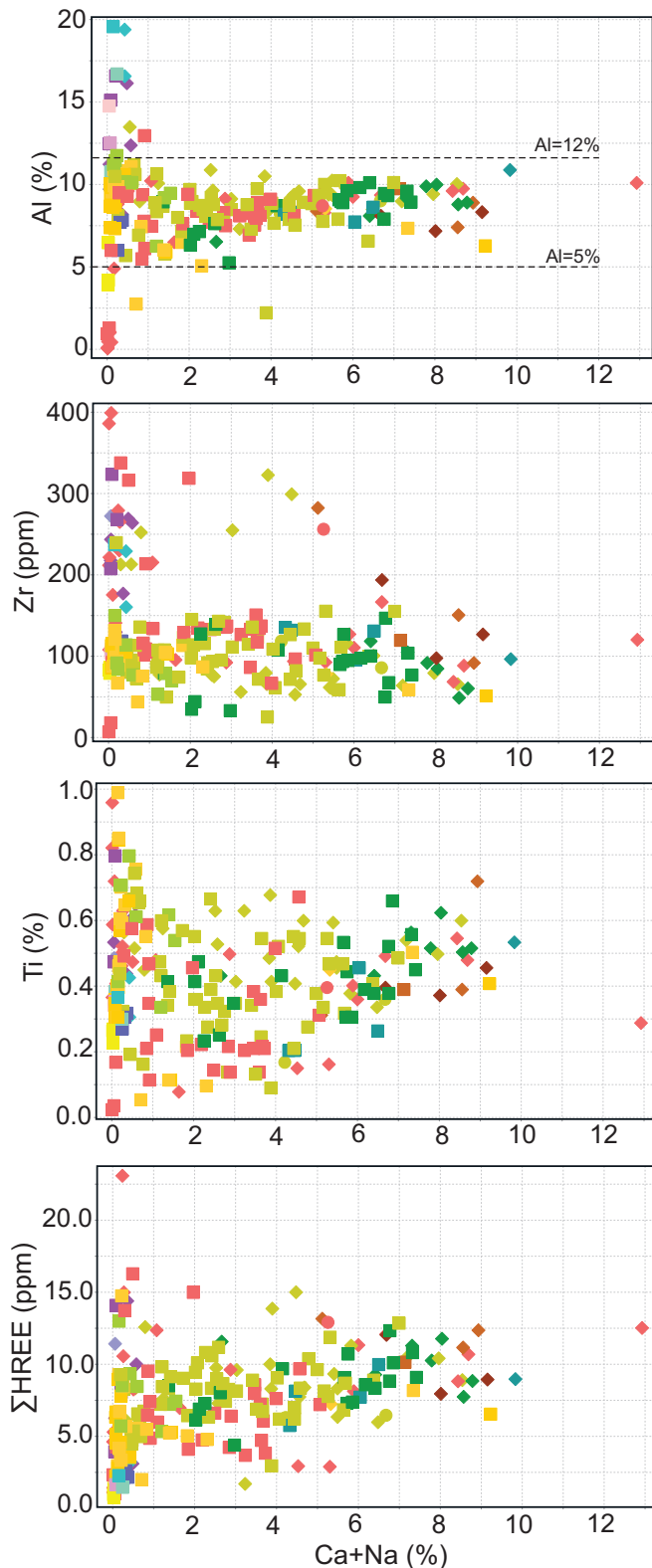


Figure 18: Scatter plots to show relative immobility of (a) Al, (b) Zr, (c) Ti, and (d) HREE based on concentration of Na+Ca. Samples are colour-coded by alteration types (see Figure 6b for the colour legend). Al concentration shows least dependence on the alteration type or intensity except at very low Na+Ca concentrations. Thus, samples with Al > 12% and < 5% are excluded for the use of Al as an immobile element.

assemblages and chemical composition of the host rocks are zoned and provide vectors towards the mineralization, it is expected that the corresponding rock physical properties could provide proxies and vectors to mineralization.

Magnetic Susceptibility

Magnetite occurs as a primary component of most of the host rocks and forms during the K-silicate alteration. However, much of the magnetite is altered to hematite during the overprinting phyllic and advanced argillic alterations. Magnetic susceptibility has a positive correlation with the Na+Ca concentration of the rock (Figure 19a), and rocks with Na+Ca concentrations >2 wt.% have higher magnetic susceptibility of >1 ($\times 10^{-3}$ SI Units), whereas rocks with magnetic susceptibility <0.1 have <1 wt.% Na+Ca. Rocks with high magnetic susceptibility have chlorite and chlorite-epidote and weak chlorite-muscovite alteration. Magnetic susceptibility decreases with an increase of muscovite alteration intensity as indicated by low Na+Ca <1. The advanced argillic altered rocks with muscovite, pyrophyllite, topaz, andalusite, corundum, and alunite alterations have magnetic susceptibility <0.1. At Tanzilla and Alunite Ridge, zones of strong advanced argillic alteration show very low magnetic susceptibility of <0.1, surrounded by rocks with low magnetic susceptibility (<1) with higher values (>10) occurring in bodies of rock more distally (Figure 20a). At Kemess North, the magnetic susceptibility shows a northward decrease toward the muscovite-clay altered zone before dramatically increasing in largely unaltered Hazelton Group rocks in fault contact with the Takla altered rocks.

Rock Density

Phyllic and particularly advanced argillic alteration cause net removal of rock components (Meyer and Hemley, 1967) with Al and Si left as residual elements. Locally, Si can be added to the rock in zones of silicification, but overall, the process of phyllic and advanced argillic alteration are expected to reduce the rock density and increase the porosity. A plot of rock density against Na+Ca concentrations, as a measure of alteration intensity, have a decrease in density with increasing alteration intensity (Figure 19b). Rocks with chlorite and muscovite-chlorite alteration have higher density. This is attributed to the addition of dense sulphide minerals such as pyrite to the altered rocks. Therefore, to use the density property as a vectoring tool, it is preferable to eliminate the sulphide-rich rocks from the dataset. By first eliminating alunite-rich samples using the K/Rb-alumina diagram and jarosite and gypsum-rich samples using the SWIR data, we can assume that all sulphur occurs in the structure of pyrite, and from that, the pyrite percentage can be calculated. A plot of rock density measurements against Na+Ca attributed by the calculated pyrite percentage from whole-rock geochemical data (Figure 19c) shows a better correlation between rock density and intensity of alteration in rocks with less than 2%

pyrite. Rocks with higher pyrite concentrations show higher density values. This is a more important issue for rocks that have very low Na+Ca concentrations. To improve the application of rock density data for vectoring, we have eliminated density data for rocks with calculated pyrite content >12.8%. Results for the remaining samples are shown in Figure 20b.

At Tanzilla, the advanced argillic alteration on the Main hill and in a smaller similar zone of the West zone produces lower density rocks (<2.5 g/cm³), but rock density increases to >2.7 g/cm³ in less-altered rocks immediately to the north and south of the main hill (Figure 20b). Most of the rocks at Alunite Ridge and East Ridge have densities of 2.5–2.7 g/cm³, with no significantly lower density zones occurring with the areas of strong alunite-clay alteration. However, rock densities are low (<2.4 g/cm³) in the central parts of the North Ridge, where muscovite is the main alteration mineral. This relationship suggests that silicification in zones of advanced argillic alteration may have

compensated for the material loss, resulting in an average rock density value, whereas in areas where silicification did not overprint phyllic or argillic alteration, rock densities are lower. The latter occurs at Kemess North, which is characterized by strong muscovite and clay alterations and by low (<2.4 g/cm³) rock densities (Figure 20b)

Rock Porosity

Rock porosity increases with the intensity of alteration (Figure 19d). Samples with biotite and chlorite alteration show low porosity (around 1%), whereas samples with advanced argillic alterations of kaolinite and dickite, alunite, topaz, andalusite, and corundum show a wide range of porosity from 1 to >10%. The scatter is probably largely controlled by silicification and overprinting clay alteration (with minimal host rock effect), which formed a locally-cemented, porous texture from the intense acid leaching during advanced argillic alteration.

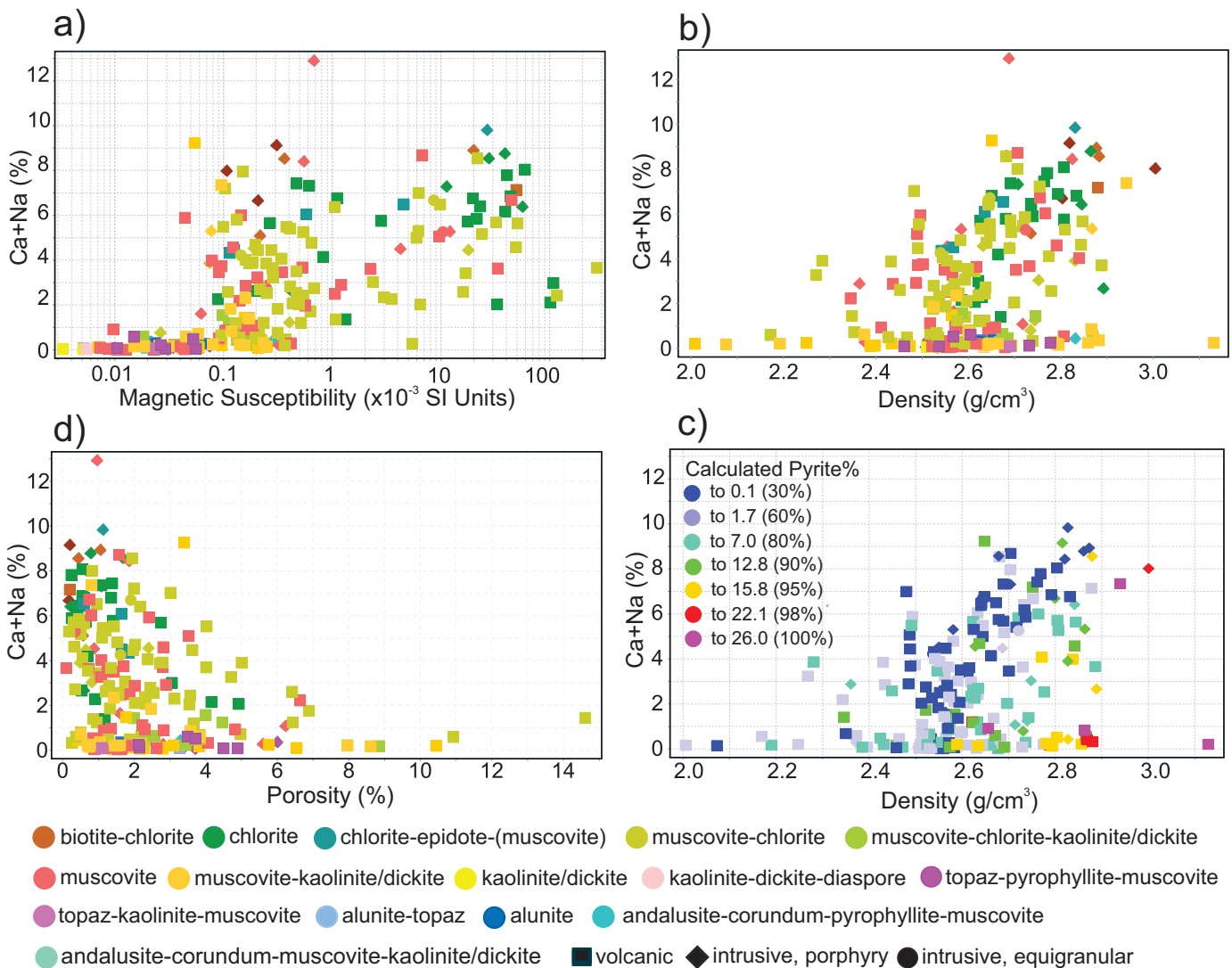


Figure 19: a) Magnetic susceptibility versus combined concentration of Na and Ca as a proxy for alteration intensity. Samples are colour-coded based on alteration type; b) rock density versus Na+Ca; c) similar to 15b but samples color-coded based on pyrite abundance; d) rock porosity versus Na+Ca.

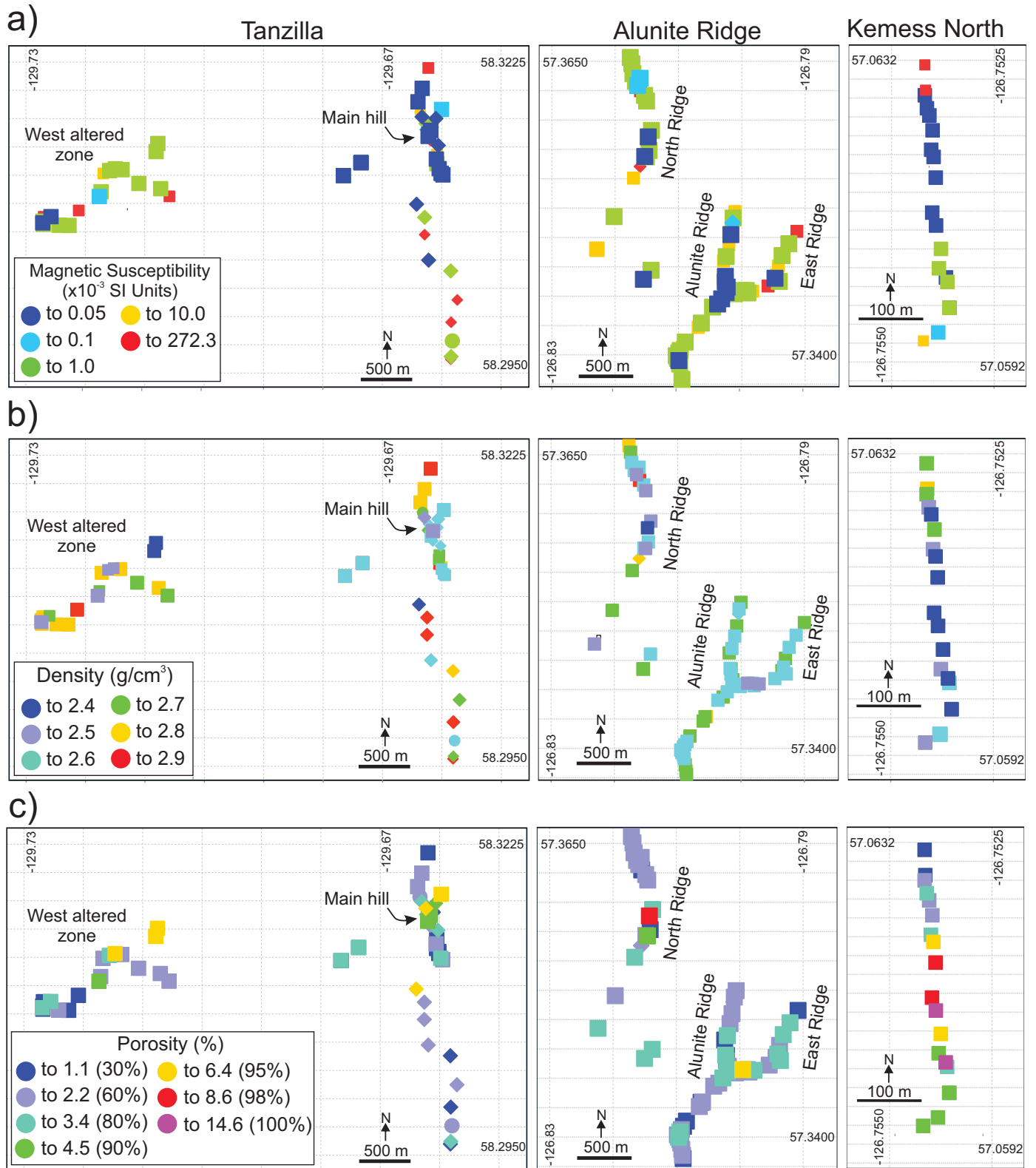


Figure 20: Maps showing sample distribution, colour-coded for: a) magnetic susceptibility; b) rock density; and c) rock porosity.

A map of rock porosity shows samples with higher porosity (>3.4%) in the central parts of Tanzilla main hill and lower porosity (<2.2%) to the north and south (Figure 20c). Similar smaller zones occur in the West zone. At Alunite Ridge, zones of rock with moderate porosity (>2.2%) occur in the central parts and continue to the East and North Ridges surrounded by rocks with lower porosity (<2.2%). At Kemess North, rocks with intense muscovite alteration in the central parts of the ridge show a very high porosity (>6.4% and locally up to 14.6%) but the porosity decrease (1.1 to 2.2%) northward in more kaolinite-dickite-rich rocks. The least altered rocks of the Hazelton Group to the north have the lowest porosity (<1.1%). This suggests that even though the type of alteration, particularly silicification and clays, will influence the rock porosity, there is a vector of increasing rock porosity towards zones of more intense alteration.

DISCUSSION: MAPPING ADVANCED ARGILLIC ALTERATION ZONING

Mineralogical and geochemical data and information can be used individually or integrated to characterize the zones of advanced argillic alteration environments in the shallow parts of the porphyry system and to provide tools that identify mineral and geochemical compositional zoning within the study sites. Variations in alteration assemblage mineralogy and geochemical

signatures suggest that the three study sites represent different levels of advanced argillic or shallow-level alteration potentially above a porphyry copper system (Figure 21).

Interpretation of alteration mineral assemblages and geochemical data suggests that sites mapped during this study represent different levels of exposure. Alunite Ridge is characterized by abundant alunite with zones of silicification and clays (kaolinite and dickite), locally minor pyrophyllite and diaspore, zones with anomalous gold and arsenic and low MPIx ratio (<3). Muscovite occurring with and around the alunite alteration shows a distinctly low crystallinity index (typically <1). Porphyry copper type vein or mineralization is not recognized at depth, but a small granodiorite body at the Sofia prospect in the Toodoggone River valley (Bouzari et al., 2020) is about 3 km northeast of Alunite Ridge (700 m lower than Alunite Ridge) and hosts porphyry type quartz-magnetite veins with K-feldspar alteration with chalcopyrite (Figure 4). Alunite Ridge, therefore, represents the shallowest setting among the study sites.

At Tanzilla, abundant pyrophyllite, topaz, and andalusite alteration occur at surface and >100–150 m below the surface. This alteration is locally surrounded by zones of alunite-rich alteration. Muscovite shows high crystallinity index (>2) at the Main Hill zone, which geochemically shows moderate MPIx ratios (around 20). Porphyry-type alteration of chlorite-

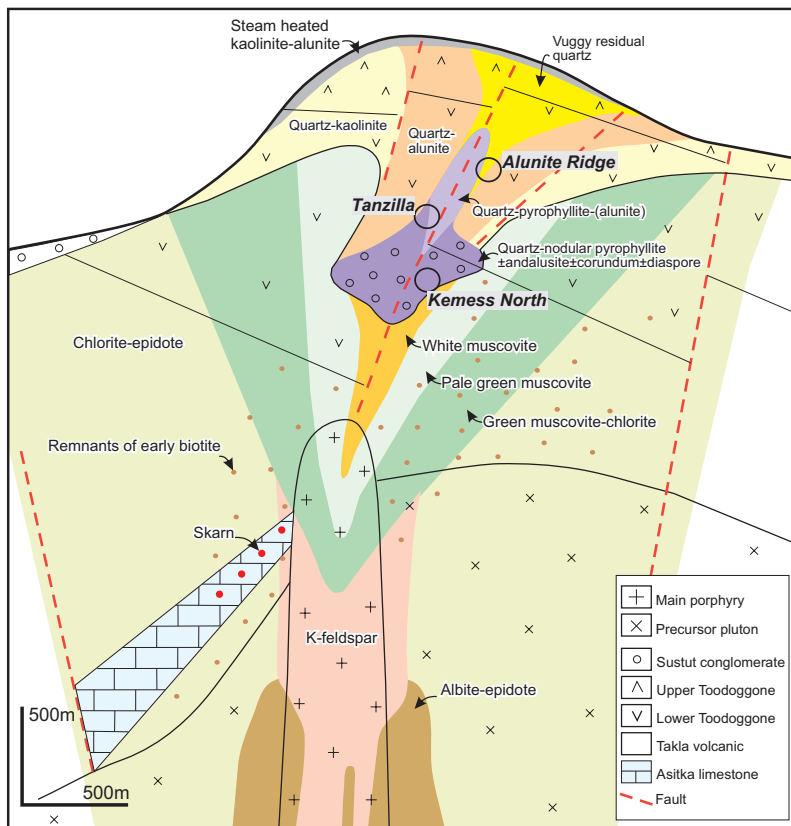


Figure 21: Schematic cross-section of porphyry systems showing host rock and alteration zoning of typical of BC alkalic porphyry deposits with their advanced argillic cap (after Sillitoe, 2010; and Hedenquist and Arribas, 2021) and approximate vertical position of the sites characterized during this study.

muscovite with weak copper mineralization (<0.1% Cu) occurs below the zones of advanced argillic alteration, with remnants of K-silicate biotite alteration typically occurring below 600m. Tanzilla, therefore, reflects a deeper advanced argillic alteration setting relative to Alunite Ridge, above a weakly mineralized porphyry centre.

Alteration at Kemess North is characterized by crystalline muscovite (>2 crystallinity index), pyrophyllite, andalusite, and corundum in the north end with the highest MPIx ratio of >40. The occurrence of a nodular pyrophyllite texture (Hedenquist and Arribas, 2021) or patchy silica (Sillitoe, 2010) with this alteration suggests proximity to the base of the advanced argillic alteration zone above porphyry-type mineralization. Porphyry-type Cu-Au mineralization with sericite-chlorite alteration and quartz veins occurs approximately 100 m below the surface at Kemess North. Therefore, near-surface exposure at Kemess North represents alteration at the base of a lithocap.

Clay-rich alteration assemblages, especially kaolinite, are absent or only occur locally in the studies sites; large zones of kaolinite alteration are absent from many areas of advanced argillic alteration in BC. This is interpreted to be the result of erosion of the shallow and low-temperature portions of the altered zone. The dominantly mafic character of the Takla or Hazelton Group volcanic rocks, which buffered the fluids, has played a role in preventing the formation of large hypogene kaolinite alteration zones. Kaolinite and dickite are, however, common in Kemess north, especially to the north end near the fault contact. Some of the kaolinite likely has a supergene origin, as weak sulphide oxidation occurs near the surface. The nodular texture of dickite-kaolinite alteration with remnants of pyrophyllite, rimmed by quartz (Figure 10d), suggests that dickite and kaolinite alteration overprinted earlier pyrophyllite alteration. Narrow zones of clay alteration continue at depth along the structures. We interpret that the clay alteration at Kemess North is a late telescoped low-temperature overprint over the pyrophyllite-aluminous-rich assemblage.

Shallow-level lateral zoning with the characteristics discussed in the following sections are argued to be useful as vectoring tools to identify trends and zoning toward the central parts of advanced argillic-alteration zones and potentially the region above the underlying porphyry copper mineralization:

Nodular Pyrophyllite and Aluminum-rich Minerals at the Core/Roots of Advanced Argillic Alteration

Regions of advanced argillic alteration are mineralogically zoned, and if defined, can be used to vector towards higher temperature portion of the system (Hedenquist and Arribas, 2021). Extensive evidence suggests that shallow lithocap alteration can be offset from the intrusive centre (Sillitoe, 1995; Hedenquist et al., 1998) along hydraulic gradients, such

that lithocaps are asymmetric in distribution and occur on the shoulders of intrusions (Hedenquist and Taran, 2013; Hedenquist and Arribas, 2021). Therefore, identifying vectors towards the core or roots of the lithocaps is critical in exploration.

Mineral assemblages containing pyrophyllite, andalusite, corundum, and/or diaspore, locally topaz, with a variable amount of muscovite, occur in more central portions and in the roots of advanced argillic altered zones in the studied sites. The occurrence of pyrophyllite with other aluminosilicate minerals that are closely associated with muscovite alteration is interpreted to constitute the hottest environment of hydrolytic alteration at the base of a lithocap and suggests a transitional environment that overlies porphyry Cu-Au orebodies such as in Far Southeast, El Salvador, and Oyu Tolgoi (Hedenquist and Arribas, 2021). An assemblage of corundum, andalusite, and diaspore indicates a temperature of >370° to 400°C, and the assemblage of andalusite and muscovite at quartz saturation suggests a slightly lower temperature, perhaps 360° to 375°C (Watanabe and Hedenquist, 2001). These zones were probably formed along sub-vertical channels originating from the porphyry-related magmatic source (Hedenquist and Taran, 2013). Alteration of andalusite to muscovite and pyrophyllite is reported in El Salvador due to cooling (Watanabe and Hedenquist, 2001). Textural relationships in this study suggest that muscovite and pyrophyllite were replaced by andalusite, probably due to an increase in temperature. Similar relationships have been shown at Cerro Colorado, where andalusite replaced coarse muscovite in the deeper part of advanced argillic alteration (Bouzari and Clark, 2006). Retrograde alteration has commonly altered the andalusite to clays at the rims.

In contrast to the pyrophyllite occurring in the base of the lithocap, pyrophyllite forms with abundant alunite at shallower parts of lithocaps from a sulfate-rich condensate of volcanic vapor (Hedenquist and Arribas, 2021). But in this shallower setting, diaspore, andalusite, and corundum typically do not occur with pyrophyllite. Therefore, when exploring in advanced argillic-altered rocks for porphyry copper mineralization at depth, the key is to identify the location of these aluminum-rich phases in association with pyrophyllite. Pyrophyllite is best identified by SWIR. Topaz and diaspore can also be identified by SWIR, but andalusite and corundum are not typically identifiable by SWIR. Pyrophyllite, typically with diaspore or corundum, replaces muscovite and quartz (Hedenquist and Arribas, 2021) and forms an alteration with characteristics nodular texture (or patchy silica) such as in Kemess North (Figure 10c). Similar textures have been described in several porphyry deposits (See Sillitoe, 2010 and Hedenquist and Arribas, 2021, and reference therein). Subsequently, the pyrophyllite might have been overprinted by clays such as dickite and kaolinite (Hedenquist and Arribas, 2021) but the nodular texture is preserved which is typically rimmed by quartz (see Figure 10d). These textures

are indicative of advanced argillic alteration transition to top of porphyry environment (Hedenquist and Arribas, 2021).

Transition from Green to White Muscovite

Aluminum-rich mineral assemblages are zoned outward to white colour muscovite and clay (kaolinite-dickite) mineral assemblage, typically with silicification. The white muscovite alteration in the studies sites is surrounded by a zone of pale-green muscovite alteration, which grades outward to zones of green muscovite-chlorite alteration. Rock colour becomes darker green with an increase in abundance of chlorite. The pale-green muscovite and green muscovite-chlorite alteration at depth at Kemess North host porphyry copper-gold mineralization. The green and pale-green muscovite alteration assemblages are probably more widespread in porphyry deposits, and their distribution is typically underestimated or mistaken for chlorite alteration typical for the propylitic zone. The pale green and green muscovite-chlorite alterations are comparable to the green sericite alteration originally described in the Philippine porphyry deposits (Sillitoe and Gappe, 1984) and subsequently elsewhere (e.g., Chuquicamata, Chile, Ossandón et al., 2001; Cerro Colorado, Chile, Bouzari and Clark, 2006). Sillitoe (2010) has recognized that the green sericite alteration is typically an early stage, whereas the white sericite is a later stage that more commonly occurs in structurally-controlled or irregular replacement zones within the upper parts of green sericite-chlorite and potassic zones.

The SWIR data shows a transition from paragonitic muscovite in a distal location to K-rich muscovite more proximal to the areas with strong advanced argillic alteration, but it is not possible to correlate this transition accurately with muscovite color. Whole-rock geochemical data, however, suggests that rocks with pale-green and green muscovite alteration typically have higher Mg/K and K/Al relative to white muscovite that has lower K/Al (Figure 15b). We interpret based on the SWIR data that much of muscovite at the shallow levels have low crystallinity, but more crystalline K-rich muscovite occurs at depth. The high K/Al (>0.33) occurring locally suggests the occurrence of relict K-feldspar or biotite (e.g., Figure 10h). Studies elsewhere (e.g., at Copper Cliff porphyry, Montana; Uribe-Mogollon and Maher, 2018) have shown that the rocks with early green muscovite alteration have phengitic composition (longer Al-OH absorption wavelength; 2,206–2,210 nm) whereas those with the late white muscovite phase are K-rich (shorter Al-OH absorption wavelength; 2,197–2,206 nm). Therefore, mapping muscovite and chlorite colour in the field, backed by whole-rock geochemical data, and recognizing the zonation provides a first-order guide to identifying the anatomy of the porphyry alteration and location of advanced argillic alteration or D-type vein clusters that may host high-sulphidation mineralization or linked to rich copper zones at depth. Ideally, a zonation from

green muscovite-chlorite to pale-green muscovite and to white muscovite-(clay) alteration is expected towards the shallower and more central portion of the system. In areas with structural complexity, such as in Kemess North, where the alteration has an asymmetric geometry, the muscovite alteration mapping will help identify and map post-mineralization displacement.

K-Mg-Alumina and K/Rb-Alumina Diagrams to Map Alteration

Field observation and SWIR data are essential in mapping alteration: however, the mineralogical changes may be difficult to see macroscopically, and SWIR has limited capacity in identifying mineral mixtures and typically cannot identify anhydrous minerals such as andalusite or corundum. Whole-rock geochemical data provide a useful tool to map alteration and can complement field and SWIR data (e.g., Halley, 2020). The alkali-alumina diagram of Davies and Whitehead (2006) does not accurately map the chlorite and muscovite alteration zones, especially in intermediate and mafic volcanic host rocks. One of the key advantages of using the Mg data is the identification of chlorite and characterization of muscovite types, especially phengitic muscovite. Samples with the phengitic chemical domain probably represent H⁺ metasomatism, during which most chlorite and biotite are altered to muscovite with phengitic composition (high Mg-Fe, Mg/K~0.1–0.2), forming the pale-green muscovite. In this environment of alteration it is common to have relict biotite and/or K-feldspar causing a high (>0.33) K/Al ratio (e.g., Figure 10h). Continued and/or overprinting H⁺ metasomatism forms the white muscovite-(clay) alteration with a significantly lower Mg/K ratio and typically K/Al ratio of less than 0.33. Therefore, use of K-Mg-alumina diagram helps to predict and map chlorite and muscovite alteration types, i.e., chlorite, green muscovite-chlorite, pale-green muscovite, and white muscovite-(clay) assemblages.

Similar to the alkali-alumina diagram, the K-Mg-alumina diagram might be affected by the rock types. We have shown above that rock types did not affect the distribution of alteration assemblages in the studies sites. The potential effects of rock types on the K-Mg-Alumina diagram are shown in Figure 14a, in which the Mg/K molar ratios are plotted against V/Sc and with samples color-coded by rock types. This diagram shows a scatter of Mg/K from high to low regardless of rock types (e.g., basaltic Takla versus dacitic tuff of the Toodoggone Formation). Similar diagram type but color-coded by alteration types (Figure 14b) shows that rock types do not cause a noticeable effect on alteration types. The diagram shows that rocks with chlorite or muscovite-chlorite alteration typically have Mg/K ratio of >0.2. Therefore, the Mg/K ratio seems to be largely controlled by alteration types, and there is no noticeable effect by the rock types.

Moreover, application of the K/Rb-Alumina diagram identifies Al-rich minerals such as andalusite and corundum from the muscovite-(clay) assemblages and provides a key tool for mapping zones of advanced argillic altered rocks. These can be supplemented by the Na-Ca depletion index, especially for areas where the zone of intense advanced argillic alteration is not exposed, to vector towards areas with high fluid flow and potentially to the more central parts of alteration above a porphyry centre. A combination of muscovite and Al-rich mineral mapping and Na-Ca depletion index from whole-rock geochemical data provides a useful tool to vector towards mineralization in advanced argillic alteration.

Rock Physical Properties

Rock physical properties, including magnetic susceptibility, density, and porosity, are affected by alteration and rock types and can be used as vectors, especially when rock types and/or sulphide contents are taken into consideration. Magnetic susceptibility and rock densities decrease towards central parts of advanced argillic alteration zones, whereas porosity commonly increases, except for weaker porosity in areas overprinted by silicification or clay alteration. Whereas the measurement of magnetic susceptibility is fast and can be done in the field, the density and porosity measurements typically require a simple laboratory setting using saturation and buoyancy techniques (Ulusay and Hudson, 2007). A reasonable estimate for sample processing is about 150 samples per day. This study showed that rock physical properties correlate with the alteration mineralogy, and therefore they can be used to recognize large alteration zoning. More importantly, the characterization of rock physical properties provides a basis on which to interpret geophysical data, which can be used for vectoring in areas where younger cover masks advanced argillic altered zones.

Trace Element Vectors: MPIx and MPIx- Lateral

Porphyry copper deposits comprise a wide range of metal tenor and a corresponding diversity of paragenesis and fabric (e.g., Clark, 1993) but commonly have large alteration and geochemical footprints (e.g., Titley et al., 1986; Cunningham et al. 2004; Halley et al., 2015; Byrne et al., 2020). Trace element geochemical data provide a useful tool to map the footprint of a porphyry deposit, but a key question is always how deep and where the potential mineralization occurs. Therefore, interpreting the geochemical data for vectoring purposes laterally or vertically becomes an important issue, especially where laterally extensive advanced argillic alteration zones, possibly asymmetric mushroom-shaped geometries with respect to a porphyry system at depth, are present (Figure 1). The application of MPIx-Lateral and MPIx demonstrates that trace element geochemical data can be used to map the lateral and vertical zonation of the porphyry system. This simple

approach provides indices to compare prospects in a district, identify size and level of exposure, and target drilling.

Red Luminescent Quartz

The luminescence colour and intensity of quartz is diagnostic of mineralizing fluid events in porphyry copper deposits and reflects the physical and chemical environment of quartz formation (Götze et al., 2004; Rusk et al., 2006, 2011). Pervasive silicification and veinlets of quartz commonly occur with pyrophyllite, and dickite-kaolinite, in silicified rocks of advanced argillic altered rocks typically shows dark red luminescence, with the pyrophyllite and clays displaying blue luminescent color. Younger generations of quartz that cut the red luminescent quartz or quartz that occur distally with green muscovite-chlorite alteration do not show luminescence (i.e., dark CL). The exception is the coarse, commonly banded quartz veins related to low to intermediate sulphidation epithermal veins at Quartz Lake near Alunite Ridge. These late veins have a yellow luminescence color.

Quartz luminescence is controlled by temperature and its trace element composition. The red luminescent quartz described in this study is comparable to the Ti-poor, late quartz at Far Southeast porphyry copper deposit, Philippine occurring with the ore-stage chlorite-sericite alteration (Bennett, 2014). Bennett (2014), based on textural evidence and fluid inclusion studies has shown that the red CL quartz formed at low temperature (<400°C) and overprinted early, blue luminescence, Ti-rich quartz, which formed at higher temperature (>400°C). Similar relationships have been shown at Butte, Montana, and porphyry and epithermal veins in Maricunga Belt, Chile (Bennett, 2014), and at Taiyangshan porphyry deposit, China (Qui et al., 2021). Maydagán et al. (2015) and Rusk et al. (2011) have shown that early-stage quartz veins in porphyry deposits (A or B veins, Gustafson and Hunt, 1975) have bright CL and are Ti-rich. As temperature decreases, Al concentrations increase, and quartz displays relatively darker CL. The yellow luminescent quartz veins at low to intermediate sulphidation epithermal veins at Quartz Lake are comparable to the late fracture-controlled euhedral quartz associated with ore minerals at Veladero high-sulphidation epithermal deposit, El Indio-Pascua belt, Argentina (Holley et al., 2017). These veins formed at a low-temperature hydrothermal environment, mostly 200°C (Holley et al., 2017), and indicate rapid precipitation in a reduced environment (Götze et al., 2015).

These observations suggest that the red luminescent quartz described here probably link with the ore stage red luminescent quartz veins that typically form with porphyry veins. Fluid inclusion data are not available and difficult to obtain due to the fine-grained nature of quartz, but given the occurrence of dickite and pyrophyllite with the red luminescent quartz, a temperature range of 200–250°C is expected. These are

overprinted and surrounded by dark luminescent quartz that occurs at a greater distance. Therefore, the characterization and identification of red luminescent quartz can be particularly useful for vectoring in areas with large quartz-clay alteration zone, making it difficult to map alteration, especially when other key high-temperature minerals are not exposed.

CONCLUSIONS

Zones of advanced argillic alteration are favourable exploration targets because they can host epithermal high sulphidation type gold and/or underlie porphyry type copper mineralization. However, mineral exploration within advanced argillic zones is difficult because of the large size of the altered areas, the intense nature of the alteration, and the subtle mineralogical changes. Three sites characterized during this study represent examples of advanced argillic altered zones in BC. The absence of large kaolinite- or alunite-altered areas suggests that much of the shallow parts of advanced argillic altered zones are not preserved in BC. However, a range of shallow to deep parts of lithocaps are preserved. At Alunite Ridge, the quartz-alunite alteration with vuggy quartz texture is an example of a shallow setting, whereas pyrophyllite-andalusite-corundum alteration with nodular textures at Kemess North developed at the base of advanced argillic alteration just above a porphyry centre. Results from this study provide several criteria and tools to map both vertical and lateral zoning within the advanced argillic altered area:

- 1. Zones of advanced argillic alteration in BC typically contain muscovite and are surrounded by muscovite-chlorite alteration.** The occurrence of muscovite probably suggests a deeper level (higher temperature) lithocap setting but may also suggest that lower temperature assemblages, such as pyrophyllite-clays, have overprinted earlier alteration (telescoping) as a result of uplift and downward collapse of the hydrothermal system (Sillitoe, 2010). Results from this study shows that the muscovite crystallinity index calculated from SWIR data provides a vector for higher temperature, central/deeper zones, of the system in BC.
- 2. Colour of the muscovite alteration can be used as a field vectoring tool.** The muscovite colour changes vertically and laterally, with respect to the main up-flow zone, from green muscovite-chlorite at depth, to pale-green muscovite and to white muscovite-(clay) alteration towards the shallower and more central portion of the system. The green and pale-green muscovites typically have phengitic composition, whereas the white muscovite is K-rich.
- 3. Whole rock geochemical data can be used to predict alteration mineralogy and zoning.** The Mg-K-Al diagram

provides a tool to map white muscovite-clay-(aluminum-rich minerals), pale-green muscovite, green muscovite-chlorite, and chlorite-dominated alteration assemblages. The white muscovite-clay-(aluminum-rich) group can be further subdivided, separating Al and alunite-rich minerals using the K/Rb-Al molar diagram.

- 4. Identification of pyrophyllite and aluminum-rich minerals such as andalusite, corundum, and diaspor provides a key component in vectoring towards porphyry copper mineralization at the base of lithocap.** These minerals can be identified in the field by nodular texture (or patchy silica) such as those in Kemess North. Pyrophyllite is best identified by SWIR, whereas aluminum-rich phases typically require petrography or whole-rock geochemical analysis. At the larger scale, the relative loss of Na and Ca can be quantified—relative to immobile Al—using the proposed index, to map the intensity of muscovite and advanced argillic alteration, and to vector towards areas with high fluid-flow and potentially to the more central parts of alteration above a porphyry centre.
- 5. Preliminary data collected during this study suggest that quartz in more central parts of the advanced argillic alteration zone displays red luminescence and typically occurs with blue luminescent pyrophyllite and clays,** whereas later overprinting and distal quartz display dark luminescence.
- 6. Rock physical properties correlate with alteration type and intensity and can be used as vectors.** Magnetic susceptibility and rock densities decrease towards central parts of the advanced argillic alteration zones, whereas porosity commonly increases. Rock physical properties provide criteria to better interpret geophysical data and explore areas where advanced argillic altered zones are partly covered by younger sediments.
- 7. Trace element geochemical data can be effectively used to map lateral and vertical vectoring components in an area with MPlx-Lateral and MPlx.** This simple approach provides indices to compare prospects in a district, identify size and level of exposure, and target drilling at depth.

ACKNOWLEDGMENTS

Geoscience BC is thanked for its financial contribution in support of this project. Kaizen Discovery Inc. gave permission to visit the Tanzilla property and sample drill core. Centerra Gold provided access to Kemess North and drill core, as well as accommodation at the Kemess mine. The authors thank Richard Billingsley for giving permission to visit the Alunite Ridge

property. Philip Lypaczewski and Benoit Rivard conducted the hyperspectral measurement, and Johanna McWhirter supplied project management. Field assistance was provided by Zina Boileau, and Bahram Najafian helped with laboratory work. We thank Shaun Barker and three anonymous reviewers for their constructive comments, which helped us to improve the report. Sara Jenkins and Beth Spencer assisted with final figures and layout.

REFERENCES

- Ague, J. and van Haren, J. (1996): Assessing metasomatic mass and volume changes using the bootstrap, with application to deep crustal hydrothermal alteration of marble: *Economic Geology*, v. 91, p. 1169–1182.
- Barker, R.D., Barker, S.L.L., Wilson, S.A. and Stock, E.D. (2021): Quantitative Mineral Mapping of Drill Core Surfaces I: A Method for μ XRF Mineral Calculation and Mapping of Hydrothermally Altered, Fine-Grained Sedimentary Rocks from a Carlin-Type Gold Deposit: *Economic Geology*, v. 116, p. 803–819.
- Barresi, T. and Luckman, N. (2016): Diamond drilling report on the Tanzilla property, northwestern British Columbia; BC Ministry of Energy, Mines and Low Carbon Innovation, Assessment Report 36431, 46 p., URL <<https://aris.empr.gov.bc.ca/ARISReports/36431.PDF>>
- Bennett, M.M. (2014): Cathodoluminescence and fluid inclusion characteristics of hydrothermal quartz from porphyry deposits. Master thesis, Colorado, Colorado School of Mines, 162 p.
- Bissig, T. and Cooke, D.R. (2014): Introduction to the special issue devoted to alkalic porphyry Cu-Au and epithermal Au deposits: *Economic Geology*, v. 109, p. 819–825.
- Booden, M.A., Mauk, J.L. and Simpson, M.P. (2011): Quantifying Metasomatism in Epithermal Au-Ag Deposits: A Case Study from the Waitekauri Area, New Zealand: *Economic Geology*, v. 106, p. 999–1030.
- Bouzari, F. and Clark, A.H. (2006): Prograde evolution and geothermal affinities of a major porphyry copper deposit: The Cerro Colorado hypogene protore, I Región, Chile: *Economic Geology*, v. 101, p. 95–134.
- Bouzari, F., Bissig, T., Hart, C.J.R., Leal-Mejía, H. and Smith, C. (2020): Porphyry mineral systems in the central Toodoggone district, British Columbia, *In* E.R. Sharman, J.R. Lang, and J.B. Chapman, eds., *Porphyry Deposits of the Northwestern Cordillera of North America: A 25-Year Update*. Canadian Institute of Mining, Metallurgy and Petroleum. Special volume 57, p. 228–252.
- Byrne, K., Lesage, G., Gleeson, S.A., Piercey, S.J., Lypaczewski, P. and Kyser, K. (2020): Linking Mineralogy to Lithogeochemistry in the Highland Valley Copper District: Implications for Porphyry Copper Footprints: *Economic Geology*, v. 115, p. 871–907.
- Chang, Z., Hedenquist, J.W., White, N.C., Cooke, D.R., Roach, M., Deyell, C.L., Garcia, J., Gemmell, J.B., McKnight, S. and Cuisson, A.L. (2011): Exploration tools for linked porphyry and epithermal deposits: Example from the Mankayan intrusion-centered Cu-Au district, Luzon, Philippines: *Economic Geology*, v. 106, p. 1365–1398.
- Clark, A.H. (1993): Are outsize porphyry copper deposits either anatomically or environmentally distinctive?, *In* Whiting, B.H., Hodgson, C.J., and Mason, R., eds., *Giant Ore Deposits: Society of Economic Geologists, Special Publication 2*, p. 213–283.
- Cooke, D., White, N., Zhang, L., Chang, Z. and Chen, H. (2017): Lithocaps – characteristics, origins and significance for porphyry and epithermal exploration: *Mineral Resources to Discover - Proceedings of the 14th SGA Biennial Meeting*, p. 291–294.
- Cunningham, C.G., Austin, G.W., Naeser, C.W., Rye, R.O., Ballantyne, G.H., Stamm, R.G. and Barker, C.E. (2004): Formation of a paleothermal anomaly and disseminated gold deposits associated with the Bingham Canyon porphyry Cu-Au-Mo system, Utah: *Economic Geology*, v. 99, p. 789–806.
- Davies, J.F. and Whitehead, R.E. (2006): Alkali-alumina and MgO-alumina molar ratios of altered and unaltered rhyolites: *Exploration and Mining Geology*, v. 15, p. 75–88.
- Deyell, C.L., Thompson, J.F.H., Friedman, R.M. and Groat, L.A. (2000): Age and origin of advanced argillic alteration zones and related exotic limonite deposits in the Limonite Creek area, central British Columbia: *Canadian Journal of Earth Sciences*, v. 37, p. 1093–1107.
- Diakow, L.J. (2001): Geology of the southern Toodoggone River and northern McConnell Creek map areas, north-central British Columbia (parts of NTS 94E/2, 94D/15 and 94D16); BC Ministry of Energy, Mines and Petroleum Resources, BC Geological Survey, Geoscience Map 2001-1, scale 1:50 000, URL <http://cmscontent.nrs.gov.bc.ca/geoscience/PublicationCatalogue/GeoscienceMap/BCGS_GM2001-01.pdf>
- Diakow, L.J., Nixon, G.T., Rhodes, R. and van Bui, P. (2006): Geology of the central Toodoggone River map area, north-central British Columbia (parts of NTS 94E/2, 6, 7, 10 and 11); BC Ministry of Energy, Mines and

- Petroleum Resources, Open file map 2006-6, scale 1:50 000, URL <http://cmscontent.nrs.gov.bc.ca/geoscience/PublicationCatalogue/GeoscienceMap/BCGS_GM2006-06.pdf>
- Diakow, L.J., Panteleyev, A. and Schroeter, T.G. (1991): Jurassic epithermal prospects in the Toodoggone river area, northern British Columbia: examples of well preserved, volcanic-hosted, precious metal mineralization: *Economic Geology*, v. 86, p. 529–554.
- Diakow, L.J., Panteleyev, A. and Schroeter, T.G. (1993): Geology of the early Jurassic Toodoggone Formation and gold–silver deposits in the Toodoggone river map area, northern British Columbia; BC Ministry of Energy, Mines and Petroleum Resources, Bulletin 86, 72 p., URL <http://cmscontent.nrs.gov.bc.ca/geoscience/PublicationCatalogue/Bulletin/BCGS_B086.pdf>
- Duuring, P., Rowins, S.M., McKinley, B.S.M., Dickinson, J.M., Diakow, L.J., Kim, Y.-S. and Creaser, R.A. (2009): Examining potential genetic links between Jurassic porphyry Cu-Au±Mo and epithermal Au±Ag mineralization in the Toodoggone district of North-Central British Columbia, Canada: *Mineralium Deposita*, v. 44, p. 463–496.
- Escolme, A., Berry, R.F., Hunt, J., Halley, S. and Potma, W. (2019): Predictive models of mineralogy from whole-rock assay data: Case study from Productora Cu-Au-Mo deposit, Chile: *Economic Geology*, v. 114, p. 1513–1542.
- Götze, J., Pan, Y., Stevens-Kalceff, M., Kempe, U., and Müller, A. (2015): Origin and significance of the yellow cathodoluminescence (CL) of quartz: *American Mineralogist*, v. 100, p. 1469–1482.
- Götze, J., Plötze, M., Graupner, T., Hallbauer, D.K. and Bray, C.J. (2004): Trace element incorporation into quartz: A combined study by ICP-MS, electron spin resonance, cathodoluminescence, capillary ion analysis, and gas chromatography: *Geochimica Cosmochimica Acta*, v. 68, p. 3741–3759.
- Gustafson, L.B., and Hunt, J.P. (1975): The porphyry copper deposit at El Salvador, Chile: *Economic Geology*, v. 70, p. 857–912.
- Halley, S.W. (2020): Mapping magmatic and hydrothermal processes from routine exploration geochemical analyses: *Economic Geology*, v. 115, p. 489–503.
- Halley, S.W., Dilles, J.H. and Tosdal, R.M. (2015): Footprints: hydrothermal alteration and geochemical dispersion around porphyry copper deposits: *Society of Economic Geologists, Newsletter*, no. 100.
- Hedenquist, J.W. and Taran, Y.A. (2013): Modeling the formation of advanced argillic lithocaps: volcanic vapor condensation above porphyry intrusions: *Economic Geology*, v. 108, p. 1523–1540.
- Hedenquist, J.W. and Arribas, A., Jr. (2021): Exploration Implications of Multiple Formation Environments of Advanced Argillic Minerals: *Economic Geology*, DOI: <https://doi.org/10.5382/econgeo.4880>
- Hedenquist, J.W., Arribas, A., Jr. and Reynolds, T.J. (1998): Evolution of an intrusion-centered hydrothermal system: Far Southeast-Lepanto porphyry and epithermal Cu-Au deposits, Philippines: *Economic Geology*, v. 93, p. 373–404.
- Heinrich, C.A. (2007): Fluid-fluid interactions in magmatic-hydrothermal ore formation: *Reviews in Mineralogy and Geochemistry*, v. 65, p. 363–387.
- Heinrich, C.A., Driesner, T., Stefánsson, A. and Seward, T.M. (2004): Magmatic vapor contraction and the transport of gold from the porphyry environment to epithermal ore deposits: *Geology*, v. 32, p. 761–764.
- Hemley, J.J., Montoya, J.W., Marinenko, J.W. and Luce, R.W. (1980): Equilibria in the system Al₂O₃-SiO₂-H₂O and some general implications for alteration-mineralization processes: *Economic Geology*, v. 75, p. 210–228.
- Hervé, M., Sillitoe, R.H., Wong, C., Fernández, P., Crignola, F., Ipinza, M. and Urzúa, F. (2012): Geologic overview of the Escondida porphyry copper district, northern Chile: *Society of Economic Geologists Special Publication 16*, p. 55–78.
- Holley, E.A., Monecke, T., Bissig, T., and James Reynolds, T.J. (2017): Evolution of High-Level Magmatic-Hydrothermal Systems: New Insights from Ore Paragenesis of the Veladero High-Sulfidation Epithermal Au-Ag Deposit, El Indio-Pascua Belt, Argentina: *Economic Geology*, v. 112, p. 1747–1771.
- Jiang, S., Wang, R., Xu, X. and Zhao, K. (2005): Mobility of high-field strength elements (HFSE) in magmatic-metamorphic-, and submarine-hydrothermal systems: *Physics and chemistry of the Earth*, v. 30, p. 1020–1029.
- Khashgerel, B.E., Kavalieris, I. and Hayashi, K. (2008): Mineralogy, textures, and whole-rock geochemistry of advanced argillic alteration: Hugo Dummett porphyry Cu–Au deposit, Oyu Tolgoi mineral district, Mongolia: *Mineralium Deposita*, v. 43, p. 913–932.
- Kuran, D.L. and Barrios, A. (2005): Geological, geochemical and diamond drilling report on the Sickie-BeeGee Claim

- Group, Toodoggone area; report prepared for Stealth Mineral Limited, BC Ministry of Energy, Mines and Low Carbon Innovation, Assessment Report 27790A, 28 p., URL <<https://aris.empr.gov.bc.ca/ARISReports/27790A.PDF>>
- Landtwing, M.R., Pettke, T., Halter, W.E., Heinrich, C.A., Redmond, P.B., Einaudi, M.T. and Kunze, K. (2005): Copper deposition during quartz dissolution by cooling magmatic-hydrothermal fluids: The Bingham porphyry: *Earth and Planetary Science Letters*, v. 235, p. 229–243.
- Large, R.R., Gemmell, J.B., Paulick, H. and Huston, D.L. (2001): The Alteration Box Plot: A Simple Approach to Understanding the Relationship between Alteration Mineralogy and Lithogeochemistry Associated with Volcanic-Hosted Massive Sulfide Deposits: *Economic Geology*, v. 96, p. 957–971.
- Li, Z.X.A. and Lee, C.T.A. (2004): The constancy of upper mantle fO₂ through time inferred from V/Sc ratios in basalts: *Earth and Planetary Science Letters*, v. 228, p. 483–493.
- Longo, A.A., Dilles, J.H., Grunder, A.L. and Duncan, R. (2010): Evolution of calc-alkaline volcanism and associated hydrothermal gold deposits at Yanacocha, Peru: *Economic Geology*, v. 105, p. 1191–1241.
- Loucks, R.R. (2014): Distinctive composition of copper-ore-forming arc magmas: *Australian Journal of Earth Sciences*, v. 61, no. 1, p. 5–16.
- Lypaczewski, P., Rivard, B., Lesage, G., Byrne, K., D'Angelo, M. and Lee, R.G. (2020): Characterization of mineralogy in the Highland Valley porphyry Cu district using hyperspectral imaging, and potential applications: *Minerals*, v. 10, Issue 5, 473 p., DOI: <https://doi.org/10.3390/min10050473>
- Maydagán, L., Franchini, M., Rusk, B., Lentz, D., Mcfarlane, C., Impiccini, A., Rios, F. and Rey, R. (2015): Porphyry to epithermal transition in the Altar Cu-(Au-Mo) deposit, Argentina, studied by cathodoluminescence, LA-ICP-MS, and fluid inclusion analysis: *Economic Geology*, v. 110, p. 889–923.
- McKinley, B.S.M. (2006): Geological characteristics and genesis of the Kemess North porphyry Au–Cu–Mo deposit, Toodoggone district, north-central British Columbia, Canada: M.Sc. thesis, The University of British Columbia, 136 p., URL <<https://open.library.ubc.ca/cIRcle/collections/ubctheses/24/items/1.0052897>>
- Meyer, C. and Hemley, J.J. (1967): Wall rock alteration; *In* *Geochemistry of Hydrothermal Ore Deposits*, H.L. Barnes (ed.), Holt, Reinhart and Winston, Inc., New York, New York, p. 166–235.
- Nelson, J. and Mihalynuk, M. (1993): Cache Creek ocean: closure or enclosure?: *Geology*, v. 21, p. 173–176.
- Ossandón, C.G., Fréaut, R.C., Gustafson, L.B., Lindsay, D.D. and Zentilli, M. (2001): Geology of the Chuquicamata mine: A progress report: *Economic Geology*, v. 96, p. 249–270.
- Panteleyev, A. and Koyanagi, V.M. (1994): Advanced argillic alteration in Bonanza volcanic rocks, northern Vancouver Island – lithologic and permeability controls; *In* *Geological Fieldwork 1993*, BC Ministry of Energy, Mines and Petroleum Resources, BC Geological Survey, Paper 1994-1, p. 101–110, URL <<https://www2.gov.bc.ca/gov/content/industry/mineral-exploration-mining/british-columbia-geological-survey/publications/fieldwork>>
- Pearce, J.A. and Norry, M.J. (1979): Petrogenetic implications of Ti, Zr, Y, and Nb variation in volcanic rocks: *Contributions to Mineralogy and Petrology*, v. 69, p. 33–47.
- Portela, B., Sepp, M.D., van Ruitenbeek, F.J.A., Hecker, C. and Dilles, J.H. (2021): Using hyperspectral imagery for identification of pyrophyllite-muscovite intergrowths and alunite in the shallow epithermal environment of the Yerington porphyry copper district: *Ore Geology Reviews*, v. 131, DOI: <https://doi.org/10.1016/j.oregeorev.2021.104012>
- Qiu, K., Deng, J., Yu, H., Wu, M., Wang, Y., Zhang, L. and Goldfarb, R. (2021): Identifying hydrothermal quartz vein generations in the Taiyangshan porphyry Cu-Mo deposit (West Qinling, China) using cathodoluminescence, trace element geochemistry, and fluid inclusions: *Ore Geology Reviews*, v. 128, DOI: <https://doi.org/10.1016/j.oregeorev.2020.103882>
- Rusk, B., Koenig, A. and Lowers, H. (2011): Visualizing trace element distribution in quartz using cathodoluminescence, electron microprobe, and laser ablation-inductively coupled plasma-mass spectrometry: *American Mineralogist*, v. 96, p. 703–708.
- Rusk, B.G., Lowers, H.A. and Reed, M.H. (2008): Trace elements in hydrothermal quartz: Relationships to cathodoluminescent textures and insights into vein formation: *Geology*, v. 36, p. 547–550.
- Rusk, B.G. and Reed, M.H. (2002): Scanning electron microscope-cathodoluminescence analysis of quartz reveals complex growth histories in veins from the Butte porphyry copper deposit Montana: *Geology*, v. 30, p. 727–730.
- Rusk, B.G., Reed, M.H., Dilles, J.H. and Kent, A.J.R. (2006):

- Intensity of quartz cathodoluminescence and trace-element content in quartz from the porphyry copper deposit at Butte, Montana: *American Mineralogist*, v. 91, p. 1300–1312.
- Sillitoe, R.H. (1995): Exploration of porphyry copper lithocaps: Pacific Rim Congress, Auckland, 1995, Proceedings: Melbourne, Australasian Institute of Mining and Metallurgy, p. 527–532.
- Sillitoe, R.H. (2010): Porphyry copper systems: *Economic Geology*, v. 105, p. 3–41.
- Sillitoe, R.H. (1999): Styles of high-sulphidation gold, silver and copper mineralization in porphyry and epithermal environments: Pacrim '99 Congress, Bali, Indonesia, Proceedings: Melbourne, Australasian Institute of Mining and Metallurgy, p. 29–44.
- Sillitoe, R.H. and Gappe, I.M., Jr. (1984): Philippine Porphyry Copper Deposits; Geologic Setting and Characteristics: Committee for Co-Ordination of Joint Prospecting for Mineral Resources in Asian Offshore Areas, UNDP technical support for regional offshore prospecting in East Asia, 89 p.
- SRK Consulting Inc. (2016): Technical report for the Kemess underground project and Kemess East resource estimate, British Columbia, Canada; report prepared for AuRico Metals Inc., 409 p., URL <https://www.centerragold.com/cg-raw/cg/KemessUG_Updated_Technical-Report_2CA046-004_20160506_FNL.pdf>
- Stanley, C.R. and Madeisky, H.E. (1996): Lithogeochemical exploration for metasomatic zones associated with hydrothermal mineral deposits using Pearce element ratio analysis: British Columbia, Canada, Mineral Deposit Research Unit, Short Course Notes on Pearce Element Ratio Analysis, 99 p.
- Steven, T.A. and Ratté, J.C. (1960): Geology and ore deposits of the Summitville district, San Juan Mountains, Colorado: U.S. Geological Survey Professional Paper 343, 70 p.
- Stoffregen, R.E. (1987): Genesis of acid-sulfate alteration and Au-Cu-Ag mineralization at Summitville, Colorado: *Economic Geology*, v. 82, p. 1575–1591.
- Titley, S.R., Thompson, R.C., Haynes, F.M., Manske, S.L., Robison, L.C. and White, J.L. (1986): Evolution of fractures and alteration in the Sierrita-Esperanza hydrothermal system, Pima County, Arizona: *Economic Geology*, v. 81, p. 343–370.
- Ulusay, R. and Hudson, J.A. (2007): *The Complete ISRM Suggested Methods for Rock Characterization, Testing and Monitoring: 1974-2006*; compiled by the ISRM Turkish National Group, International Society for Rock Mechanics, ISRM Commission on Testing Methods, 628 p.
- Uribe-Mogollon, C. and Maher, K. (2018): White mica geochemistry of the Copper Cliff porphyry Cu deposit: Insights from a vectoring tool applied to exploration: *Economic Geology*, v. 113, p. 1269–1295.
- van Straaten, B.I. and Bouzari, F. (2018): The Middle Jurassic Tanzilla–McBride hydrothermal system: one of the largest lithocaps in BC?: Mineral Exploration Roundup, Vancouver, BC, January 22–25, 2018, poster presentation.
- van Straaten, B.I. and Gibson, R. (2017): Late Early to Middle Jurassic Hazelton Group volcanism and mineral occurrences in the McBride–Tanzilla area, northwest British Columbia; *In Geological Fieldwork 2016*, BC Ministry of Energy, Mines and Petroleum Resources, BC Geological Survey, Paper 2017-1, p. 83–115, URL <http://cmscontent.nrs.gov.bc.ca/geoscience/PublicationCatalogue/Paper/BCGS_P2017-01-06_vanStraaten.pdf>
- van Straaten, B.I. and Nelson, J.L. (2016): Syncollisional late Early to early Late Jurassic volcanism, plutonism, and porphyry-style alteration on the northeastern margin of Stikinia; *In Geological Fieldwork 2015*, BC Ministry of Energy, Mines and Petroleum Resources, BC Geological Survey, Paper 2016–1, p. 113–143, URL <http://cmscontent.nrs.gov.bc.ca/geoscience/PublicationCatalogue/Paper/BCGS_P2016-01-07_vanStraaten.pdf>
- van Straaten, B.I., Gibson, R. and Nelson, J. (2017): Preliminary bedrock geology of the Tanzilla and McBride area, British Columbia; BC Ministry of Energy, Mines and Petroleum Resources, BC Geological Survey, Open File 2017-9, scale 1:50 000, URL <http://cmscontent.nrs.gov.bc.ca/geoscience/PublicationCatalogue/OpenFile/BCGS_OF2017-09.pdf>
- Watanabe, Y. and Hedenquist, J.W. (2001): Mineralogic and stable isotope zonation at the surface over the El Salvador porphyry copper deposit, Chile: *Economic Geology*, v. 96, p. 1755–1797.
- Williams, N. and Davidson, G. (2004): Possible submarine advanced argillic alteration at the Basin Lake prospect western Tasmania, Australia: *Economic Geology*, v. 99, p. 987–1002.

LIST OF APPENDICES

Digital Appendix 1: Sample list, location and description (.xlsx)

Digital Appendix 2: Hyperspectral data (.xlsx)

Digital Appendix 3: SWIR hyperspectral mineral maps (.pdf)

Digital Appendix 4: Whole rock geochemical data (.xlsx)

Digital Appendix 5: Rock physical property data (.xlsx)